Physics of Fluids

RESEARCH ARTICLE | JANUARY 02 2024

Tracking plume-regolith interactions in near-vacuum conditions

S. Subramanian ; A. Wilson ; C. White ; K. Kontis ; D. Evans; J. Van den Eynde

Check for updates

Physics of Fluids 36, 013301 (2024)
https://doi.org/10.1063/5.0180669

View Online
Export Citation
CrossMark

12 February 2024 09:19:23

AIP Advances
Why Publish With Us?
25 DAYS average time to 1st decision
740+ DOWNLOADS average per article
INCLUSIVE scope
Learn More
AIP Publishing

AIP Publishing

Physics of Fluids ARTICLE pubs.aip.org/aip/pof

Tracking plume-regolith interactions in near-vacuum conditions

Cite as: Phys. Fluids **36**, 013301 (2024); doi: 10.1063/5.0180669
Submitted: 11 October 2023 · Accepted: 30 November 2023 ·
Published Online: 2 January 2024

View Online Export Citation CrossMark

S. Subramanian,[1,a)] A. Wilson,[1] C. White,[1] K. Kontis,[1] D. Evans,[2] and J. Van den Eynde[3]

AFFILIATIONS

[1]James Watt School of Engineering, University of Glasgow, Glasgow G12 8QQ, United Kingdom
[2]Fluid Gravity Engineering Ltd., The Old Coach House, 1 West Street, Emsworth, Hampshire PO10 7DX, United Kingdom
[3]ESA-ESTEC, Keplerlaan 1, Noordwijk 2201 AZ, The Netherlands

[a)]Author to whom correspondence should be addressed: s.subramanian.1@research.gla.ac.uk

ABSTRACT

An experiment to track and measure the transient phenomenon of plume-liberated regolith in near-vacuum conditions was performed in a dedicated plume-regolith facility housed at the University of Glasgow. This facility with a total volume of around 82 m^3 can simulate a soft or hard landing event on "extraterrestrial" sub-atmospheric pressures. Particle image velocimetry method was used to estimate the ejection velocity and ejected angle of regolith particles, and its limitations are discussed. Glass microspheres that are matched with the size of the Lunar and Martian moon "Phobos" surface regoliths are used as simulants. With an exit Mach number of 6.6, a heated convergent–divergent nozzle represents the lander nozzle. Preliminary results capture ejecta development up to 30 ms from plume impingement. Flow visualization reveals the initial moments of plume boundary growth and regolith ejection. The vector images indicate a triangular-shaped sheet of particles sweeping from the regolith bed at a positive inclination with a local maximum velocity close to 100 m/s. The low-density "Phobos" simulant advances at a higher speed, reaches higher elevations, and covers a larger spatial area compared to a higher-density "Lunar" simulant. Observation of the crater formation reveals the difference in cohesive forces between the selected simulants. A higher inclination of particle ejection of more than 50° adjacent to the jet indicates particle entrainment originating from the interior of the crater. Stream traces reveal the deflection of ejected particles upon impingement on the lander surface at close proximity.

© 2024 Author(s). All article content, except where otherwise noted, is licensed under a Creative Commons Attribution (CC BY) license (http://creativecommons.org/licenses/by/4.0/). https://doi.org/10.1063/5.0180669

12 February 2024 09:19:23

I. INTRODUCTION

During Lunar soft landings, the ejection of dust/regolith from landing sites can interact with the lander's instruments, potentially causing problems. Apart from obstructing an astronaut's visibility of the Lunar surface during the landing maneuver,[1] the sharp-edged Lunar soil particles ejected at high speed from the impingement of the jet from the lander nozzle can damage equipment such as solar panels, optics, moving joints, navigation sensors, and transmission antennae in the vicinity of the rocket impingement.[2] The sharp-edged soil particles are the byproducts of the absence of natural weathering for millions of years in a near-vacuum environment.[3] The regolith dust clouds and the reflected jet flow may also have an effect on the spacecraft's force and torque balance. In addition, the liberated dust and plume can also cause electromagnetic interference (brownout),[4] such as the sporadic velocity errors detected by the radar telemetry during the final descent stage of the Mars Science Laboratory. These errors were attributed to the motion of surface material that was kicked up by the thruster plumes of the descending sky crane.[5] Therefore, it is of utmost importance to understand the dynamics of the ejected particles resulting from the nozzle plume impingement in order to predict the potential damage that may be caused to lander instruments and nearby installations in future missions. Despite several advancements in numerical and experimental techniques, our understanding of the characteristics pertaining to the interaction between plumes and regolith remains constrained due to its multiphase nature and complexity in replicating the extraterrestrial factors in the terrestrial environment.

In recent decades, there have been significant advancements in computational methods that have allowed for the prediction of the ejection velocity and angle of particles liberated by plumes in rarefied environments. Morris *et al.*[6] adopted a hybrid direct simulation Monte Carlo (DSMC) solver to model the influence of a 1-m tall fence on the ejected particle velocity at varying distances from the landing pad. He *et al.*[7] studied the interaction between rocket plumes with an exit Mach number of 6.7 at a 7 m standoff distance and Lunar regolith

© Author(s) 2024

with an average diameter of 70 μm using a two-phase DSMC simulation in Lunar atmospheric conditions. Their results show that the final velocity of particles can reach up to an average value of 50 m/s with a peak velocity of 100 m/s. Furthermore, they conclude that the particles undergo acceleration and convection to elevated temperatures in regions characterized by augmented gas density and velocity.[7]

In another numerical study conducted by Morris *et al.*,[8] a hybrid Navier–Stokes/DSMC solver was used for the gas flow and a DSMC solver for the solid phase flow were both taken into consideration to simulate axisymmetric plume impingement and dust dispersion on the Lunar surface.[8] It was observed from the simulation that particles measuring 800 nm in size were propelled to a maximum velocity of roughly 1000 m/s and subsequently eroded outward at minimal ejection angles.[9] White *et al.* developed and implemented a hybrid Navier–Stokes/DSMC approach to model the exhaust emanating from a rocket exhaust in the vicinity of a low-gravity, airless celestial body.[10] Simulation of the near field plume-regolith interaction of complicated Lunar lander configuration using a first-order Navier–Stokes–Fourier (NSF) model and particle-based discrete phase model (DPM) conducted by Rahimi *et al.* reveals the role of the Stokes number in deciding the ejection angle. The correlation between the particle diameter and the inclined angle is negative for a Stokes number less than 1 and positive for a Stokes number greater than 1.[11] Furthermore, the study pertains to the analysis of particle ejection from small craters that eject at high angles and impact lander components.

A recent addition to the development of plume surface interaction (PSI) simulation includes the NASA-funded predictive simulation capability (PSC) element of the Game Changing Development Plume Surface Interaction (GCD PSI) project.[12] This project aims to simulate PSI in Martian (650 Pa) and Lunar (vacuum) ambient environments to forecast PSI reliably and accurately. The GCD PSI's ultimate objective entails developing models that can effectively capture the interactions between gas and particle clouds, which are appropriate for implementation in the loci/gas granular flow Solver.[12] Cao *et al.* developed a *dsmcFoamPlus*[13] based solver, *rarefiedMultiphaseFoam*, in OpenFOAM and tested it in steady and transient cases for use in two-phase rarefied problems.[14] The authors updated the solver to account for solid–solid interactions and applied it to rocket exhaust plume-Lunar regolith interactions.[15] Zhang *et al.* built a simulation model to study the interaction between plumes and regolith using ground experiment results and landing picture data from the Chang'E-5 mission.[16] The results from numerical research provide an estimation of liberated particle velocities in the range between 200 and 1500 m/s for grain sizes ranging from 250 to 500 μm.[17]

It should be highlighted that these numerical models can, to varying degrees, take into account vacuum, Lunar surface temperature, and Lunar gravity, all of which are challenging to achieve in labs on Earth. The boundary conditions, numerical techniques, and physical assumptions taken also affect the simulation outcomes. Despite numerical improvements in particle movement prediction, a thorough understanding of the mechanism underlying plume-regolith interaction is still lacking due to the limited availability of practical and experimental data.[18] Reproducing the exact extraterrestrial conditions in an Earth-based laboratory still poses a major challenge. While it is possible for researchers to closely replicate the nozzle, regolith, and atmospheric characteristics, the introduction of "extraterrestrial" reduced gravity in a terrestrial laboratory is unfeasible. Therefore, the determination of ejected particle properties in an Earth-based laboratory continues to present a significant challenge for researchers due to the influence of the aforementioned terrestrial factors.

The earliest experiment to study the plume-regolith characteristics under vacuum conditions was carried out by Land and Clark[19] and Land and Scholl.[20] These experiments used a scaled-down model to represent the Apollo-era Lunar module (LM) during descent. Jaffe attempted to calculate the velocity and angle of ejected regolith utilizing the limited data obtained from the Apollo Lunar program and ground-based test outcomes.[21] During the LM landing of Apollo 12, the ejection of the Lunar regolith caused erosive damage (sand-blasting) to certain components of the Surveyor III Lunar probe, which was located a distance of ~150 m from the landing site. Based on the discoloration pattern on Surveyor's camera, an impact velocity of greater than 70 m/s and an emission angle parallel to the ground were postulated.[21] However, the ejecta velocity was later re-estimated to be between 300 and 2000 m/s in an analysis report published by NASA in 1972.[22] An experimental study was conducted in 2014 to conclude that the erosive wear is greater than 70% on reflective surfaces at moderate velocities of ~105 m/s.[23]

NASA conducted an experimental study in 2008 to assess the impact of Lunar simulants on various materials. The experiment involved the use of a sandblaster to propel the simulant particles at velocities ranging from 50 to 90 m/s.[24] A similar study was conducted by Buhler to measure the impact of the released Lunar dust on the engineering substrate through the acceleration of Lunar simulant particles ranging from 450 to 560 μm in grain size to a velocity of 200 m/s.[25] The particle velocity in the experiment was chosen from numerical results.[17] An attempt was made to utilize a drop tower technique for investigating crater formation in a reduced gravity environment, albeit limited by the dimensions of the available facility.[26] The Ejecta STORM apparatus was developed with the purpose of quantifying the velocity of the expelled particles through the utilization of laser and camera technology.[27]

The Physics Focused Ground Test (PFGT) has been developed by NASA with the aim of generating experimental data that can be used to predict the behavior of PSI in Lunar and Martian environments.[28] In connection with this, a subscale inert gas test has been developed to facilitate the validation of PSI environments and enhance comprehension of the importance of essential parameters. The test employs heated nitrogen gas as the plume stimulant and utilized different regolith simulants for the granular phase.[29] In the latest visualization study conducted at NASA Marshall Space Flight Center, a vacuum chamber measuring 15 ft was utilized for erosion studies. The findings revealed the presence of deep craters in the Martian environment and wide, shallow craters in the Lunar environment.[30] The study explores the influence of background pressure, nozzle mass flow rate, and crater shape on the formation of ejecta tracks.[31] The recent addition in the pursuit of knowledge in understanding the plume surface interaction is the development of payload stereo cameras for Lunar plume surface studies by NASA to reconstruct three-dimensional crater formation using a multiple camera photogrammetry system that will gather stereo images both during and after the Lunar lander's descent. This payload will be traveling to the moon as part of NASA's commercial payload services program.[32]

From the above survey, it is evident that despite several attempts to access the ejection velocity and ejection angle of regolith particles by

12 February 2024 09:19:23

© Author(s) 2024

both numerical and experimental attempts, there is still uncertainty among the scientific community regarding the precise estimation of these parameters during extraterrestrial touchdown. In the likelihood of sending multiple crewed and cargo missions with higher engine thrust in the coming decades, with landing sites close to one another to construct a permanent base on the moon,[33,34] it is of the utmost significance to understand, on a fundamental level, the dynamics of the ejected regolith from the interaction with lander rocket engine exhaust. Toward this goal, the present research attempts to use the particle image velocimetry (PIV) technique in an Earth-based laboratory to track the liberated regolith particles during the initial phase of propulsive landing under Lunar and small airless body environmental conditions. For this purpose, regolith simulants of different densities were chosen to replicate the physical properties of the chosen extraterrestrial objects. Realistic background pressure and nozzle Reynolds number were utilized to simulate the extraterrestrial landings. The preliminary analysis shows the present method is successful in capturing the vectors of the initial moment of the ejected regolith in a vacuum environment. An attempt is made to calculate the velocity and angle of the liberated regolith particles, and the results are discussed. Nevertheless, the accuracy of these results can be confirmed through the replication of the precise experimental conditions in subsequent simulations. To the best of the author's knowledge, some attempts made in recent years to quantitatively assess the particle velocity using optical diagnostic systems,[18,31] and there is currently no dedicated scientific literature available on the utilization of PIV for the purpose of characterizing plume-regolith interaction. In this context, the present study represents a significant advancement in comprehending the interaction between plumes and regolith through terrestrial experiments.

II. METHODOLOGY

A. Plume-regolith facility

To achieve the extraterrestrial atmospheric pressure conditions, the present research utilized a European Space Agency-funded, large volume, near-vacuum, plume-regolith facility, with a total volume of $\sim 82\,m^3$, housed at the Aero Physics Laboratory, University of Glasgow, as shown in Fig. 1, with a schematic of the facility shown in Fig. 2. With the current pump set, the ultimate pressure of the system is just under 1 Pa, which can represent atmospheric pressure on extraterrestrial airless bodies. The volume of the facility is separated into two separate compartments: the test chamber, as shown in Fig. 1, which is an axisymmetric chamber of $12\,m^3$ volume with optical and electrical access ports, and a buffer tank combined with a conductance pipe, with a volume of $70\,m^3$. The introduction of mass during nozzle operation leads to a rise in the background pressure inside the test chamber, thus altering the temporal evolution of the plume size. Due to the restricted pumping capacity, the background pressure inside the chamber rises steadily. The background gas pressure can be estimated from[35]

$$P_b = \frac{\dot{m}_p R_b T_b}{S(P_b)}, \tag{1}$$

where $\dot{m}_p$ is the mass flow removed from the test chamber through the vacuum pump, R_b and T_b are the gas constant and temperature of the background gas inside the test chamber, and $S(P_b)$ is the pumping speed as a function of background pressure. With the current pump set, the pumping speed is very small compared to the mass injection, and so the pressure will continually rise as mass is added.

FIG. 1. Test chamber of the plume-regolith test facility.

The size of the plume undisturbed by the background pressure inside a confined test chamber, L_p, can be calculated using the equation provided by Driftmyer:[35,36]

$$L_p = \frac{D_e}{2} M_e \sqrt{\gamma \left(\frac{P_e}{P_b}\right)}, \tag{2}$$

where D_e, M_e, and P_e are the diameter, Mach number, and pressure at the nozzle exit, respectively, γ is the ratio of specific heats, and P_b is the background pressure inside the chamber.

For a nozzle exit pressure of 405 Pa and an exit Mach number of 6.6, the plume is undisturbed by the back pressure for $L_p = 700$ mm when the background pressure is 1 Pa and $L_p = 220$ mm when the background pressure is 10 Pa. The maximum width of the plume can be estimated to be half of L_p, a minimum of 110 mm in the current work, which is smaller than the regolith tray diameter of 450 mm. Additionally, the stand-off height of the nozzle exit from the regolith surface is fixed at 35.6 mm, which is well within the limit of the calculated L_p values. From this observation, it is concluded that the impact of the plume on the regolith should resemble that in a pure vacuum at the specified stand-off height, particularly in the vicinity of impingement centerline.

12 February 2024 09:19:23

© Author(s) 2024

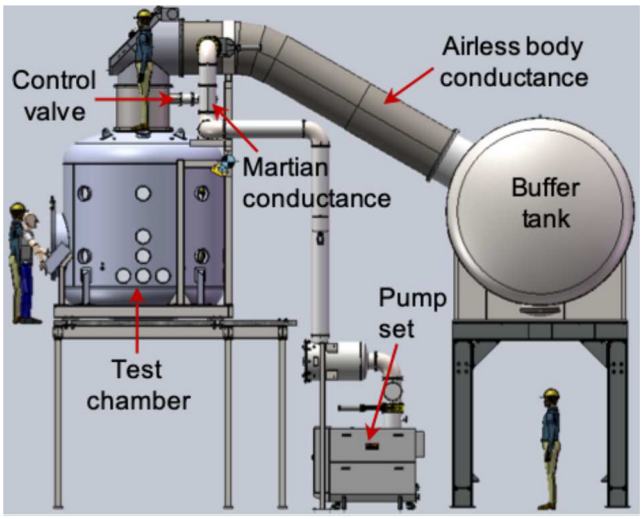

(a) Side view[37].

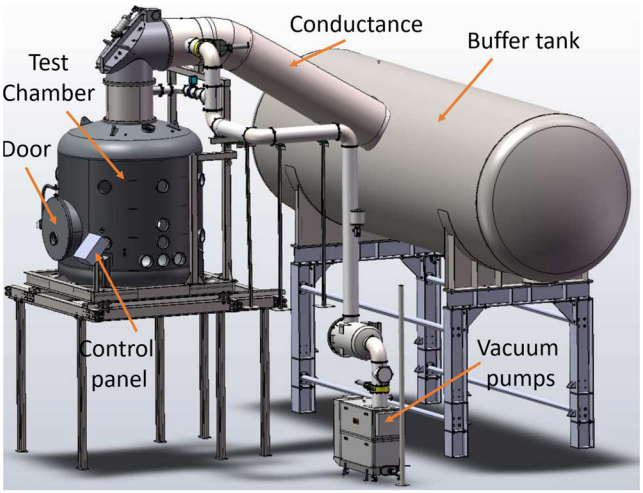

(b) Isometric view.

FIG. 2. Schematic of the plume-regolith test facility housed at the University of Glasgow.[37]

B. Regolith simulants

A 45 cm diameter × 7 cm depth plastic tray was filled up to the rim with regolith simulants representing an "extraterrestrial soil bed" and fixed under the nozzle at a height of $Y/D_e = 4$, where D_e is the diameter of the exit of the nozzle and Y is the height of the nozzle exit above the regolith tray. The tray dimensions were chosen to permit plume/regolith interaction to occur with minimal interference from an impermeable backing material.

The selection of an appropriate material to serve as a regolith simulant holds significant importance in the present investigation. The Lunar regolith is a loose, clastic substance that is primarily composed of mechanically disintegrated basaltic and anorthositic rocks. It has a fine-grained texture and ranges in color from dark gray to light gray, exhibiting some degree of cohesiveness, and its size varies depending on the specific location on the Lunar surface.[38] King *et al.* conducted grain size analyses on regolith samples obtained from the landing sites of Apollo 11 and Apollo 12.[39] The regolith from the older Apollo 11 site was discovered to have a finer grain size on average compared to the regolith collected from the Apollo 12 site. The difference in grain size was ∼16 μm. The average grain size for the latter was determined to be between 108 and 52 μm. McKay *et al.* analyzed soils that exhibit a range of mean grain sizes spanning from ∼40 to 800 μm, with an average falling within the 60–80 μm range.[40] Graf produced a guidebook including data from the Apollo and Luna missions on lunar soil particle size. There were 287 analyses of 143 different samples provided. Statistical data were obtained using graphic measures and shown for each sample. There was considerable fluctuation, although modal values around the 60 μm radius mark were typical.[41] Stoeser *et al.* provided the design specifications for a regolith simulant that was specifically created to mimic the highland material found at the landing site of Apollo 16. Multiple particle size distributions were presented, with the median particle size being ∼60 μm.[42] Gundlach and Blum proposed a technique for estimating the grain size of planetary regolith based on remote measurements of thermal inertia. A reasonable agreement was obtained for the Moon's measurements with Apollo 11. It was predicted that the average grain size would be 48 μm. It was observed that the size of regolith grains showed an inverse relationship with the mass of the planetary body.[43]

On the selection of regolith simulant to represent Lunar and small airless body conditions, Schrader *et al.* provided a detailed account of the process involved in creating numerical indicators that can be used to assess the accuracy of a regolith simulant.[44] These characteristics are addressed by:

1. Composition;
2. Particle size distribution;
3. Particle shape;
4. Particle density.

In contrast to most experiments on the effects of extraterrestrial regolith particles on flow fields during planetary entry, in which gravitational forces are negligible, the simulation of surface behaviors will require a realistic representation of the gravitational field. Due to the significantly weaker gravity on the extraterrestrial bodies being considered, it will be necessary to greatly reduce the density in order to achieve an equivalent weight. The remarkably low density required for Phobos becomes readily evident from Table I. It is highly improbable that this value can be achieved by simply reducing the density, as the simulant will lose accuracy in terms of mass and composition when the density is lowered to simulate the effects of reduced gravity. In addition, it was found that there exists a linear correlation between the specific cutting resistance and gravity.[45] This implies that simply

TABLE I. Gravitational factors for different bodies.

Environment	Gravitational factor
Earth	1.00
Lunar	0.165
Phobos	0.000 591

12 February 2024 09:19:23

© Author(s) 2024

decreasing the density of a regolith simulant is insufficient to accurately represent the impacts of reduced gravity. Hence, it is not feasible to fully fulfill the particle density, and hence the composition under typical terrestrial circumstances. Safety considerations also prevent the reduction in particle size to close a match. Particle shape may be the most straightforward to match.

The utilization of conventional regolith simulants such as JSC-1 is impeded by the relatively low density (0.511 g/cm^3) of lunar regolith. Glass microspheres represent a potential alternative. These microsphere particles may not accurately represent the overall particle shape; however, the mare regions' basalts do contain a considerable amount of glass particles that could potentially be well-matched with glass microspheres. 3M is involved in the production of various products,[46] including a selection that aligns with the aforementioned specifications. Among these, the K46 grade stands out as the most suitable option as a Lunar regolith simulant,[37] characterized by a density of 0.46 g/cm^3 and a median particle size of 40 μm (see Table II).

There is a lack of direct measurements pertaining to the Phobos regolith. According to research findings, a suitable range for representative size is between 10 and 100 μm.[47] The extremely low density required by gravitational scaling may seem impractical, but there are microspheres available, such as 3M K1, that are slightly lighter (see Table II), than those typically used for simulating Lunar regolith.

It is worth noting that the selected regolith must also be heat-resistant and have a low thermal conductivity characteristic due to its close proximity to the heated nozzle. The thermal conductivity of glass particles used in this study is 0.153 and 0.047 W/mK, which is low enough to resist the radiated heat from the nozzle.

Another important property to consider while selecting an appropriate regolith simulant is particle cohesion (Van der Waals forces). In general, it can be observed that the Lunar regolith exhibits greater cohesion compared to the terrestrial regolith. This can be attributed to the interlocking nature of the particles' irregular and occasionally reentrant surfaces.[48] Lunar regolith has not undergone physical weathering processes typically experienced on Earth, contributing to its cohesive properties.[49] Additionally, the absence of adsorbed gases on the particles further enhances the cohesion of the Lunar regolith. In the case of smaller celestial bodies, the cohesive forces overcome the low gravitational forces of the body and maintain the porosity in the regolith layer.[50]

The regolith simulants that were chosen for this experiment, specifically the hollow glass microspheres, demonstrate a certain level of cohesion, visible from the formation of clumps and fissures after a plume impingement. The variation in cohesion among the simulants used in this experiment can be confirmed through the formation of the crater at the end of the plume's impingement, as depicted in Fig. 3.

TABLE II. Regolith simulant properties.

Regolith properties	High density	Low density
Product name	3 M K46	3 M K1
Median diameter (μm)	40	65
Effective top diameter (μm)	80	120
True density (g/cm^3)	0.46	0.125
Thermal conductivity (W/mK)	0.153	0.047

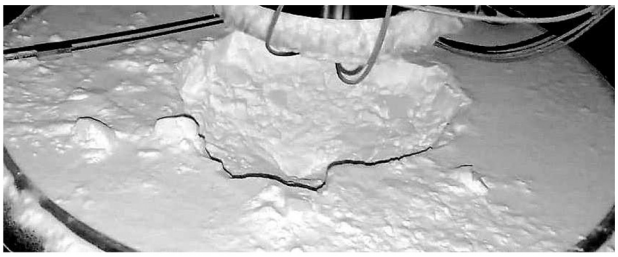

(a) Crater formation on higher density regolith (K46).

(b) Crater formation on lower density regolith (K1) - note the crater is so deep we can see the backing material.

FIG. 3. Crater formation after plume-regolith impingement.

These photographs [Figs. 3(a) and 3(b)] were captured following the restoration of atmospheric conditions within the chamber, enabling access to its interior through the opening of the chamber door. The exposure of particles to the terrestrial atmosphere reduces the cohesive property of the particles due to the absorption of water vapor from the atmosphere;[51] however, the low-pressure condition inside the test chamber removes the water vapor, thereby increasing the shear strength of the simulants.

The cohesive property is observed to exhibit a positive correlation with particle density[48] and particle size.[52] Hence, the Lunar regolith simulant, characterized by its higher density and larger size, is expected to exhibit a heightened degree of cohesion and internal friction relative to the Phobos regolith simulant with its lower density and smaller size. The presence of distinct steep walls in the high-density regolith simulant, shown in Fig. 3(a), suggests that the particles possess the ability to uphold vertical structures similar to Lunar regolith. This is in contrast to the inclined crater walls observed in the case of low-density simulants shown in Fig. 3(b). Furthermore, the high-density simulant displays the presence of clumps and fissures that are not observed on the surface of the low-density simulant. The observed reactions suggest the existence of significant cohesive forces similar to Lunar and small airless bodies among the selected simulants. This disparity in physical properties between the two simulants can potentially impact the outcome of the plume-regolith interaction.

C. Nozzle and heater assembly

The nozzle used in this study is a scaled version of a simple conical supersonic convergent–divergent nozzle with fixed convergent–divergent angles. The nozzle throat diameter is 1 mm with a tolerance of ±0.02 mm and an exit diameter of 8.94 mm. The nozzle was connected to a pressurized nitrogen supply via a regulator and a mass flow

12 February 2024 09:19:23

© Author(s) 2024

meter. The exit Mach number is 6.6. The entire nozzle assembly is mounted on an extruded aluminum-based support frame, as shown in Fig. 4. The nozzle assembly can be traversed in all three axes along the support frame. To match the exit Reynolds number with full-scale conditions, such that it can be used to simulate the plume-regolith interaction under vacuum pressure, the total temperature of the nitrogen gas is raised. This is done by attaching a heater system between the gas supply pipe and the nozzle inlet. The heater system consists of a copper matrix shaft with parallel heat channels and a heater bundle. The matrix shaft is 10 cm long and 1.6 cm wide and consists of 70 heater channels, each 1 mm in diameter, for the gas flow, as shown in Fig. 5. The copper matrix is heated by a heater bundle fixed around its circumference. The application of copper flakes between the copper bundle and matrix shaft enhances surface contact and guarantees effective heat transfer. The temperature of the heater assembly is monitored via a k-type thermocouple attached to the heater bundle and regulated by employing a proportional–integral–derivative (PID) controller (BriskHeat X2-120JTP model) on the heaters. A separate k-type thermocouple measures the gas temperature inside the nozzle stagnation chamber. Furthermore, the heater bundle is insulated from the surroundings to prevent and minimize radiation losses, as shown in Fig. 4. Section IV A provides the theoretical basis for heating nitrogen gas to an elevated temperature. With a stagnation pressure of 10 bars and a stagnation temperature of 900 K, a mass flow rate of 1 g/s is achieved.

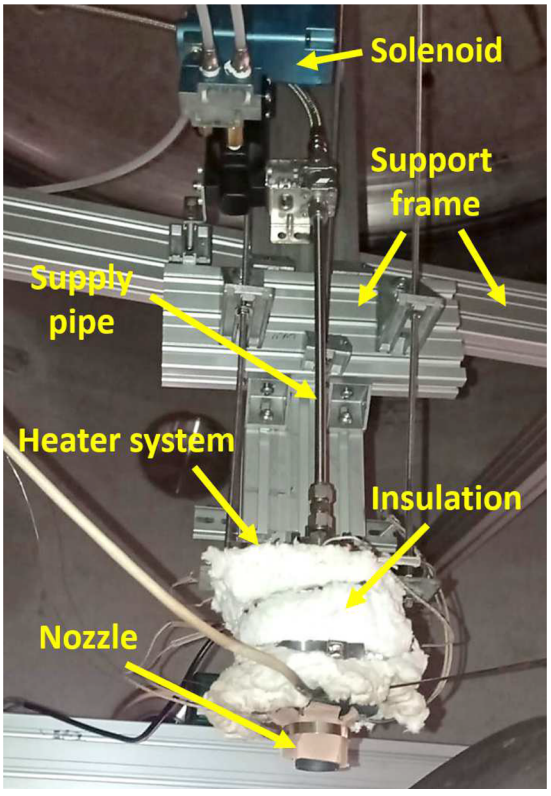

FIG. 4. Nozzle and heater assembly.

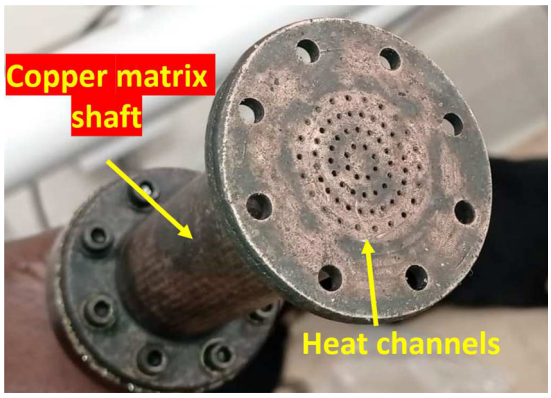

FIG. 5. Copper matrix with heat channels.

D. PIV setup

Unlike a traditional seeding approach where the freestream is seeded with reflective particles, this experiment utilized the reflective property of regolith simulants (glass particles) to track the plume-regolith interaction. Regolith particles were ejected from the regolith tray by the impingement plume, allowing them to be tracked by laser illumination through the PIV system. The schematic of the entire experimental setup with the PIV system is shown in Fig. 6.

1. Laser

The laser used was a double-pulsed Litron LDY301 ND:YLF laser (527 nm) operating at 1.5 kHz. At this frequency, the laser produces ∼10 mJ per pulse. A series of mirrors was used to direct the laser, in the correct orientation, to the experimental area within the test chamber. A mirror alignment tool was used to align the independently pulsed laser output such that it is coaxial before being directed through a semi-cylindrical lens of effective focal length (−15 mm) to produce a laser sheet of sheet thickness of 1–2 mm. The sheet was aligned such that it was parallel to the center of the jet axis.

2. Camera

To record the PIV images, a Photron APX-RS high-speed camera was fixed orthogonal to the jet axis and laser plane at a distance of ∼1500 mm. The camera was equipped with a Samyang 135 mm wide lens, which focused on the experimental area and had a low f-number to allow the maximum amount of light to enter the camera sensor. A TSI LaserPulse Synchronizer model 610035 was used to synchronize the laser and camera, with commercial software (Insight 4G) used to define the timing setup. The camera recorded at a rate of 3000 fps, meaning the PIV system captured 1500 image pairs per second, resulting in a time interval of 0.66 ms between each PIV capture.

3. Exposure settings

Due to the high reflectivity of the glass particulate, the different densities of microsphere seeders present a distinctive challenge. In order to acquire high-quality images, the laser energy power and the focal length have been adjusted for each case. The sensor resolution is

12 February 2024 09:19:23

© Author(s) 2024

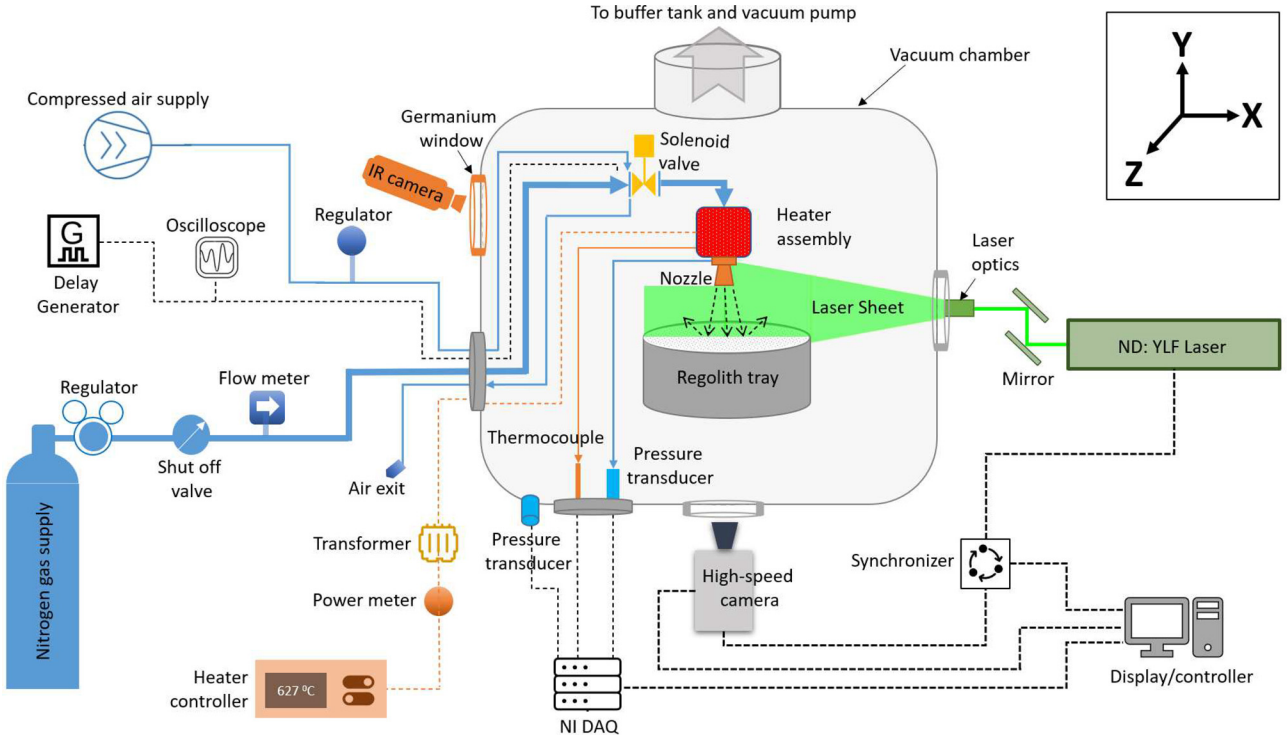

FIG. 6. A schematic of the experimental setup (inset: axis system).

set to a maximum in order to obtain the highest possible resolution from the camera at the specified frame rate of 3000 fps. In addition, the absence of an atmosphere inside the test chamber changes the way particles scatter light. Consequently, methods of trial and error involving various combinations of camera and laser parameters were tried for each case.

III. LIMITATIONS

A. Illumination asymmetry

The flow exiting the nozzle exhibits axisymmetry with respect to the y-axis, which runs vertically through the nozzle's center and causes the displacement of regolith particles in all directions. However, the PIV data obtained from the passage of a planar laser sheet visualize the ejection of particles only in a two-dimensional x–y plane. As the laser sheet is projected from one side of the optical windows of the facility (see Fig. 6), a difference in illumination in the x–y plane of the experimental area is created between the far and near sides of the laser. This difference in illumination is evident, as depicted in the raw PIV image of regolith ejection at 4 and 10 ms from the moment of jet impingement in Figs. 7(a) and 7(b).

In both the raw PIV images, the laser beam enters the image from the right side, resulting in a greater degree of illumination on the right side regolith ejection, leaving the left-side ejected particles in the shadow region. The shadow progressively expands in the following frames until it completely obscures the visual field after a certain duration. As time progresses, the PIV system's ability to accurately capture individual particles on the left side diminishes due to the concurrent expansion of the shadow region. To visualize this phenomenon, the angle of ejected particles is computed along a horizontal line at $Y/D_e = 2$ from the regolith surface, and the result is plotted in Fig. 8. The ejection angle appears to be symmetric at 4 and 6 ms meaning the laser beam can illuminate both sides at the early stages of ejecta development, attaining magnitudes of 10°–20° on each side of the impinging jet. However, in the subsequent frames, the temporal evolution of the inclination of ejected particles reveals an asymmetry due to the unevenness in illumination. Specifically, during the 8 and 10 ms

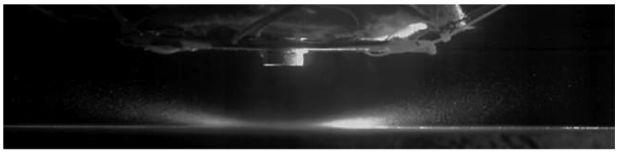

(a) 4 milliseconds from the moment of impingement.

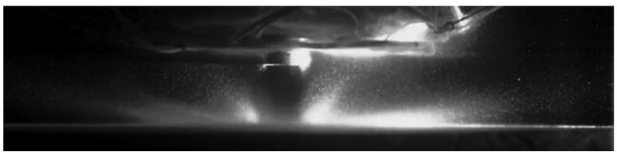

(b) 10 milliseconds from the moment of impingement.

FIG. 7. Raw images showing the difference in laser illumination at various instances of regolith ejection at $Y/D_e = 4$ stand-off height.

12 February 2024 09:19:23

© Author(s) 2024

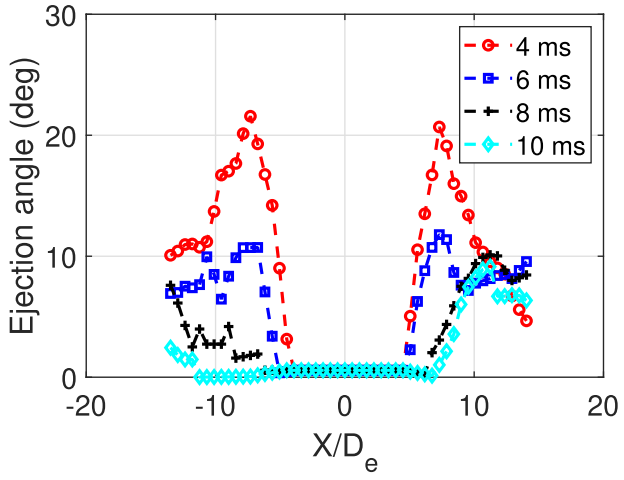

FIG. 8. Ejection angle of particle ejection plotted along a line at $Y/D_e = 2$ from the regolith surface at different time steps (nozzle center is at $X/D_e = 0$.).

intervals, the bright side displays an ejection angle of 10°, whereas, for the shadowed site, the observed ejection angle seems to decrease toward zero. This is not physical but related to the limitation of accurately observing the shadowed side. Considering this limitation, only the PIV results from the brighter side, i.e., the incoming side of the laser beam, are discussed in the rest of the article.

B. Timescale

The PIV method can acquire acceptable velocity vectors for up to 30 ms from the moment of impingement. There are two major constraints on the timeframe that lead to this limitation:

1. For an ejected velocity of ∼100 m/s in a vacuum environment, the ejected particle can return to the experimental area in about 30 ms after striking the test chamber walls at a distance of 1.5 m.
2. The accumulation of particles on the brighter side causes saturation of the pixels beyond the 30 ms time scale. The saturation region initially forms near the jet impingement region and spreads across the entire image in subsequent frames, causing velocity data to be lost for more than 50% of the image at a time of 30 ms.

IV. RESULTS AND DISCUSSION

Figure 9 shows the repeatability of chamber pressure, nozzle stagnation pressure, and temperature for two different runs.

Prior to the beginning of the investigation, the baseline pressure of the test chamber is pumped down to 1.6 Pa, representing near-vacuum conditions, and the temperature of the nozzle stagnation chamber is raised to match the exit Reynolds number to be more representative of that found in real nozzles. A delay generator with a timed trigger activated a solenoid valve and a fast-acting double-actuated ball valve located inside the vacuum chamber to initiate the nozzle firing. The actuators are installed close to the nozzle to prevent total pressure loss due to wall friction. Upon valve activation, high-pressure nitrogen gas enters the copper matrix channels surrounded by heater elements. The heated pressurized gas then enters the nozzle

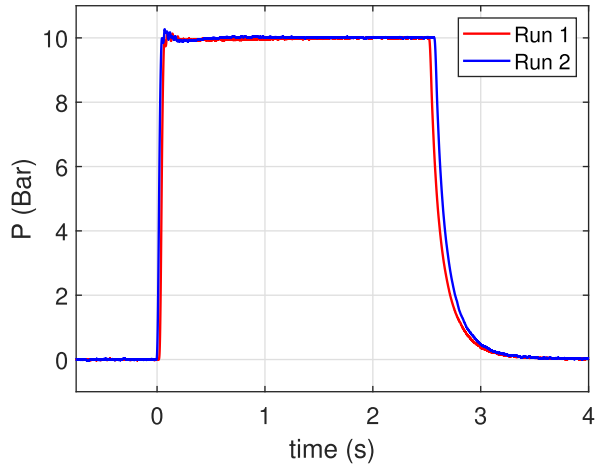

(a) Nozzle stagnation pressure.

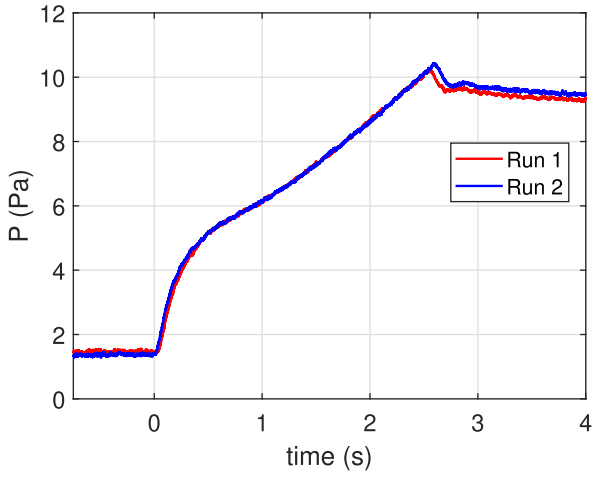

(b) Chamber pressure.

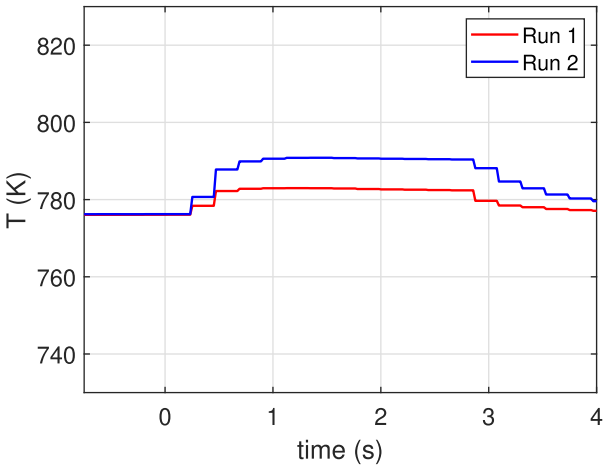

(c) Stagnation temperature of the gas in the nozzle.

FIG. 9. Measured parameters during the experiments. The results are presented for two different runs, showing the repeatability.

12 February 2024 09:19:23

© Author(s) 2024

stagnation chamber, and a total pressure of 10 bar is achieved [Fig. 9(a)]. The pressure differential between the stagnation chamber and test chamber produces a supersonic plume via the nozzle exit.

As soon as the plume is released, the test chamber pressure begins to rise, but the addition of the buffer tank ensures the rise in chamber pressure is contained within an acceptable level. At a steady 1 g/s mass flow rate, the test chamber pressure increases to 10 Pa from 1.6 Pa in 2.5 s [see Fig. 9(b)]. However, due to the current ability of the PIV system to capture only the initial moments of flow development, the rise of pressure inside the chamber at the end of the steady jet is not deemed a significant issue. Figure 9(c) shows the measured gas stagnation temperature, which is below the 900 K that the copper matrix shaft of the nozzle has been heated to, possibly due to the insufficient surface area to heat the gas up fully, but the temperature rise achieved is deemed suitable for Reynolds number similitude. It is important to emphasize that the use of the PID controller ensures that the heater bundle reaches a temperature of 900 K before firing the nozzle.

A. Reynolds number similitude

It is crucial that the facility-scale nozzle exhibit realistic nozzle flow physics in comparison to the full-scale nozzle since the actual propellant used in the full-scale motors is different from the working gas of the facility-scale motor. When the full-scale combustion chamber pressure is used, the facility scale Reynolds number is too high for cold gas. This is because low chamber temperatures result in high-density flows. Additionally, the low-temperature flow results in an increased mass flow rate compared to heated gas, which in turn presents challenges in maintaining optimal vacuum levels within the test chamber. Raising the temperature of the working gas can reduce the Reynolds number of the facility-scale nozzle flow, as well as maintain a low mass flow rate inside the test chamber.

When heat is added externally, a portion of the flow's energy excites the vibrational modes of diatomic molecules in the nitrogen gas resulting in a change in the specific heat capacity. Despite the lower temperature dependence of specific heat capacity for nitrogen, measuring 1.35 at 900 K, the accuracy of the result can be increased by considering the gas as calorically imperfect but thermally perfect. For a calorically imperfect gas, the specific heat ratio (γ) with the inclusion of the gas molecule's vibrational mode correction can be expressed as

$$\gamma = 1 + \frac{\gamma_{cp} - 1}{1 + (\gamma_{cp} - 1)\left[\left(\frac{\theta}{T}\right)^2 \frac{e^{\theta/T}}{(e^{\theta/T} - 1)^2}\right]}, \tag{3}$$

where θ is a thermal constant equal to 3056 K and subscript *cp* denotes calorically perfect conditions.

For an exit Mach number of 6.6 and for a total temperature addition of 900 K, the calorically imperfect gas equations provide the values $\frac{T}{T_0} = 0.106$, $\frac{P}{P_0} = 3.378 \times 10^{-4}$, $\frac{\rho}{\rho_0} = 0.003\,17$. It is assumed that the γ value has increased back to 1.4 by the time the gas has expanded to Ma = 6.6 at the exit and the area ratio $\frac{A}{A^*}$ for the facility scale nozzle is 80 based on the nozzle's actual dimensions.

We know from the experiment that $P_0 = 10$ bar and $T_0 = 900$ K. This gives $\rho_0 = 3.741\,\text{kg/m}^3$ and exit plane static properties of the nozzle $P_e = 337.8$ Pa, $T_e = 95.4$ K, and $\rho_e = 0.01185\,\text{kg/m}^3$. At the specified exit temperature, the use of a power law viscosity model, incorporating the properties specific to nitrogen, yields a calculated viscosity value of 7.4444×10^{-6} Pa s. From the static temperature and Mach number, the velocity is calculated as 1314.39 m/s. These properties give a Reynolds number of 9352 based on the exit radius of 4.47 mm.

If the above procedure is repeated for a total temperature of 300 K for the same total pressure, the exit plane properties of the nozzle will be T = 30.89 K, viscosity = 3.3019×10^{-6} Pa s, $\rho_e = 0.03818\,\text{kg/m}^3$, and V = 748.11 m/s, for a Reynolds number of 38 668. From this, it is evident that heating the facility scale nozzle can considerably reduce the Reynolds number of the exit flow.

B. Visualization

Visualizing the jet plume will give crucial information about the initial moment of shock/plume impingement and development. An attempt was made to conduct a visualization experiment utilizing the Schlieren technique to capture the structure of the shock and plume. The near-vacuum environment is characterized by a low refractive index, resulting in a noisy image with a barely discernible shock wave. Alternatively, a visualization of regolith particles using laser illumination was performed, and the results are presented below.

1. Jet plume

A distinct approach was employed to visualize the initial transient moment of the jet plume, and the results are presented. In this method, a thin film of low-density simulant (3M K1) tracer particles is applied to the inner walls of the divergent portion of the nozzle prior to the experiment. Once the nozzle is fired, the ejected tracer particles are subjected to illumination by a laser beam and subsequently recorded by a high-speed camera. Using this method, the growth of the plume expansion for the initial few milliseconds of the flow can be successfully captured, as shown in Fig. 10.

By using this visualization technique, it is possible to estimate the angle of the plume expansion. The angle between the nozzle centerline and the plume boundary, α (see Fig. 11), can be measured at ∼12° at the onset of the process in Fig. 10(a). As the plume develops, this angle gradually increases to 17°, 22°, and 32° approximately at time intervals of 1.32, 1.98, and 2.64 ms in Figs. 10(b)–10(d), as measured using the image processing tool in MATLAB. The expansion of the plume results in an increase in the impingement radius on the regolith bed, which ranges from $X/D_e = 1.2$ at 0.66 ms to $X/D_e = 2.7$ at 2.64 ms. At a duration of ∼8 ms, the plume is fully expanded, resulting in a curved boundary, as depicted in Fig. 10(e). The angle denoted by α attained a value exceeding 60°, while the radius of impingement increased to 6.4 times the characteristic length D_e. The plume's interaction with the regolith surface also resulted in the liberation of particles, which were ejected at an angle β, as depicted in Fig. 11. During the initial moment of impingement, the ejection angle, β, is ∼15°, but it increases to nearly 45° at ∼8 ms.

2. Regolith ejection

The ejection of regolith simulant resulting from plume impingement has been successfully visualized through the illumination of ejected simulant particles using a pulsed laser synchronized with a high-speed camera, as shown in Figs. 12–17. For visualization purposes, the nozzle location is set to the left side of the image such that the full ejection region is covered by the Samyang 135 mm lens. This gives a

12 February 2024 09:19:23

© Author(s) 2024

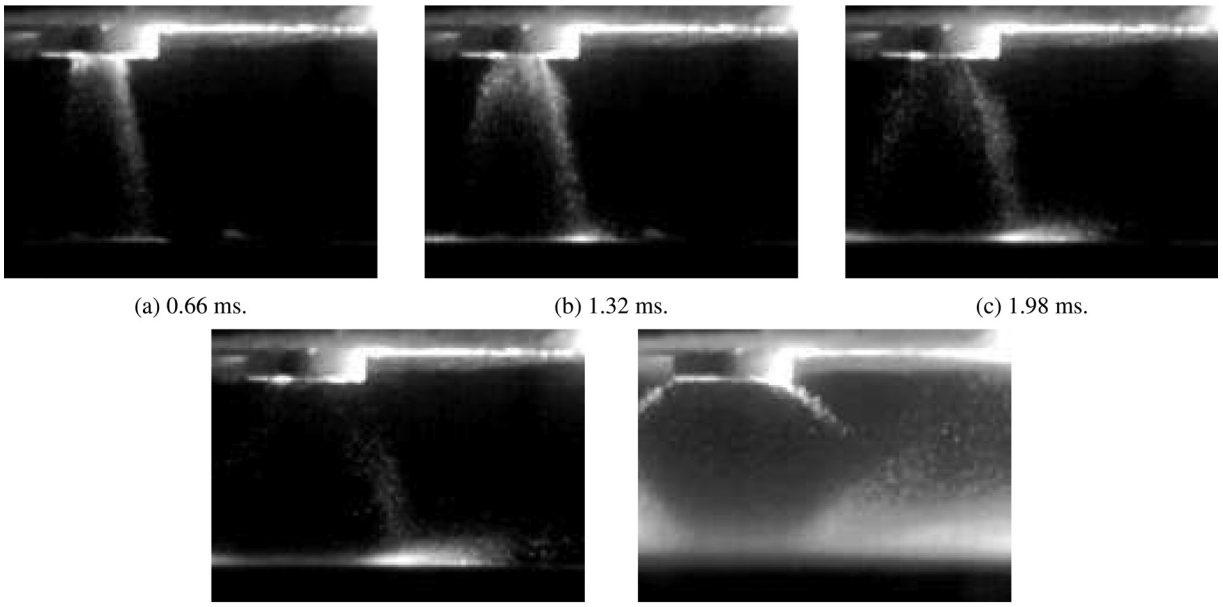

(a) 0.66 ms. (b) 1.32 ms. (c) 1.98 ms.

(d) 2.64 ms. (e) 8.58 ms.

FIG. 10. Transient visualization during the initial stages of the nozzle firing.

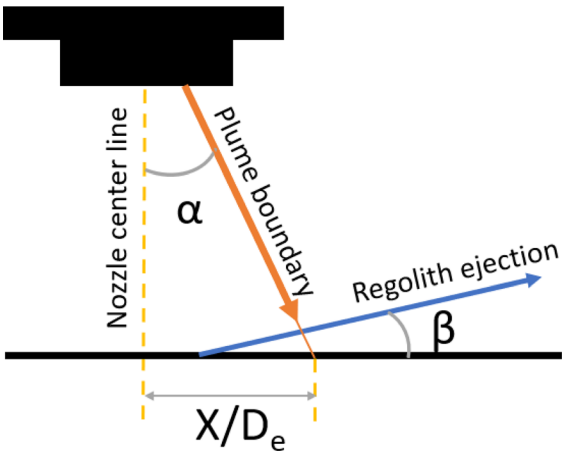

FIG. 11. Schematic of plume interaction.

field of view of approximately $X/D_e = 35$ between the nozzle center and the right side end of the frame. The laser also illuminates the edge of the tray, rendering it visible in the raw images. The intensity of reflected light from regolith particles has been enhanced by adding a processed color map alongside each unprocessed raw image. Depending on the increase in pixel intensity, the color changes from blue to red.

As shown in Fig. 12, the first sign of regolith ejection can be seen at 0.66 ms, when a small number of particles from the regolith surface can be seen on either side of the impact plume. In the succeeding frames, the expulsion appears as a sheet of particles in a triangular shape that expands in the direction away from the nozzle as seen in Figs. 13–15. A maximum angle of 12° is measured from the regolith surface in Fig. 15. As the surface area of the sheet increases, the particles in close proximity to the surface accumulate, leading to the saturation of pixels. The red coloration in the heat map serves as evidence of this.

At the time interval of 8 ms, as depicted in Fig. 16, an additional ejection event can be observed in close proximity to the plume boundary, exhibiting an ejection angle of more than 40°. In the following frame depicted in Fig. 17, the ejection at a high angle exhibits further

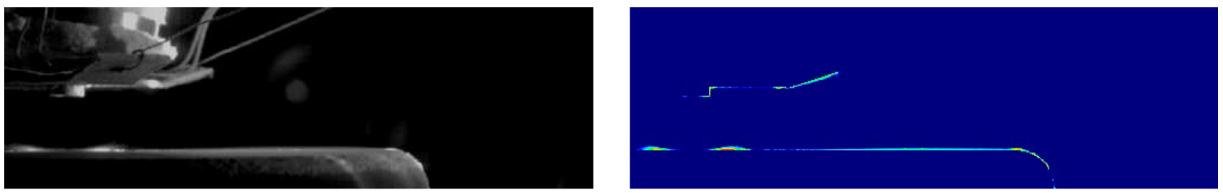

(a) Raw image from camera. (b) Color map of reflected light intensity.

FIG. 12. 0.66 ms from the moment of plume impingement on the regolith surface.

12 February 2024 09:19:23

© Author(s) 2024

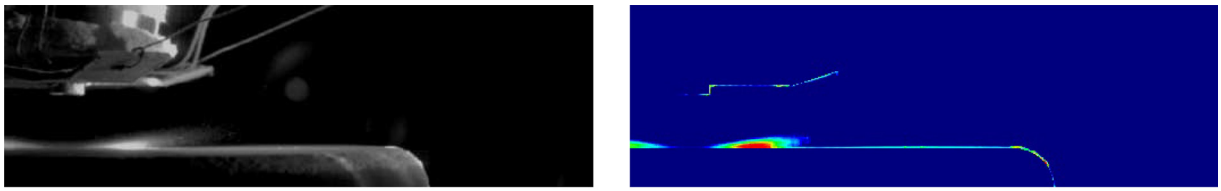

(a) Raw image from camera. (b) Color map of reflected light intensity.

FIG. 13. 2 ms from the moment of plume impingement on the regolith surface.

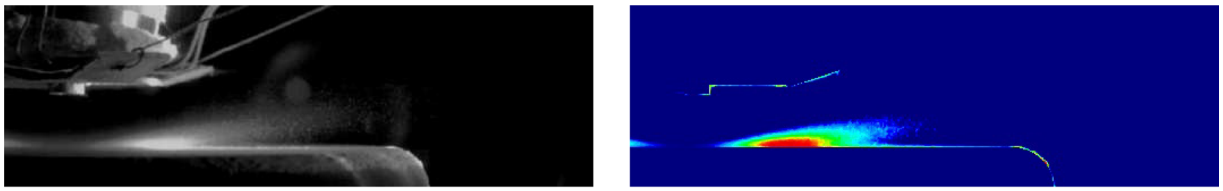

(a) Raw image from camera. (b) Color map of reflected light intensity.

FIG. 14. 4 ms from the moment of plume impingement on the regolith surface.

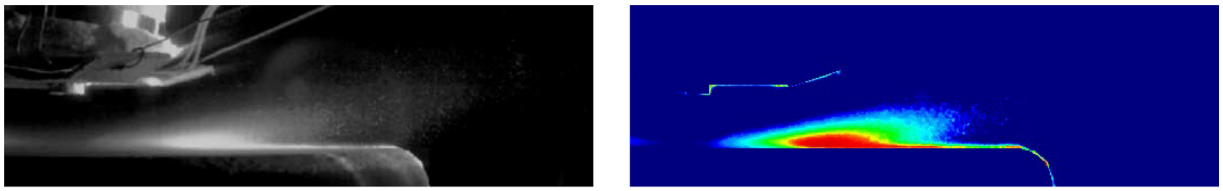

(a) Raw image from camera. (b) Color map of reflected light intensity.

FIG. 15. 6 ms from the moment of plume impingement on the regolith surface.

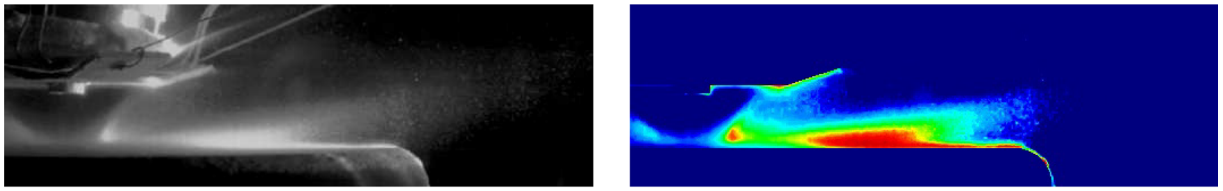

(a) Raw image from camera. (b) Color map of reflected light intensity.

FIG. 16. 8 ms from the moment of plume impingement on the regolith surface.

upward growth and collides with the lower surface of the nozzle assembly. The heat map depicted in Fig. 17(b) reveals that the area beneath the nozzle, characterized by a blue shade, exhibits a reduced concentration of regolith, which can be attributed to the downward force exerted by the jet plume. Conversely, the neighboring red region is indicative of a greater number of regolith particles that are expelled at high angles. The augmentation of the regolith concentration in proximity to the surface is also observable in Fig. 17(b).

While the use of high-speed cameras in the visualization study offers certain observations regarding the ejection angle of the plume-liberated regolith, a more detailed investigation of the particle ejection angle, relying on PIV vectors, has been discussed in Sec. IV F of this article.

C. Pressure measurement

A study was carried out to measure the pressure profile of the plume impingement in order to gain an understanding of its initial transient state. For this purpose, a circular aluminum plate with a diameter of 45 cm was fabricated with pressure tappings arranged radially from the center. The top surface of the plate is secured at a stand-off distance of $4\,D_e$ from the nozzle exit with the aid of an extruded aluminum rig. A Kulite transducer was installed in a flush-mounted configuration at the middle of the plate and was aligned with the axis of the nozzle to determine the initial moment of impingement. The nozzle is heated to 900 K and operated for a continuous 2.5 s in a near vacuum environment.

12 February 2024 09:19:23

© Author(s) 2024

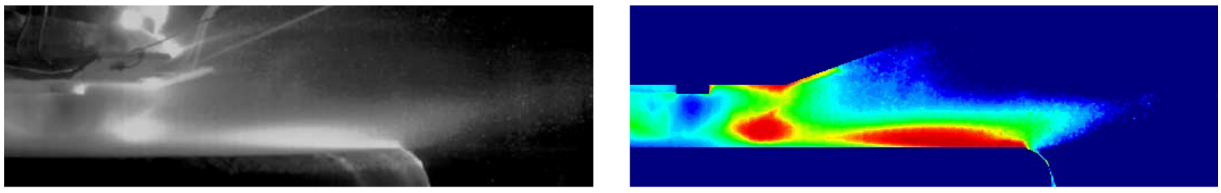

(a) Raw image from camera. (b) Color map of reflected light intensity.

FIG. 17. 10 ms from the moment of plume impingement on the regolith surface.

For a measuring frequency set to 1000 Hz, the pressure data for each millisecond have been obtained, and the results are presented in Fig. 18. A peak in pressure observed during the initial impingement indicates the presence of a starting shock wave. Subsequently, the pressure decreases gradually and stabilizes at an approximate constant magnitude after1 s from the nozzle firing, as seen in Fig. 18(a). Given that the images acquired through PIV have a limited duration of a few milliseconds from the onset of plume impingement, it is desirable to investigate the rate at which the impingement pressure attains $P/P_{max} = 1$. Figure 18(b) captures the initial pressure variations up to 35 ms. Evidently, based on the plot in Fig. 18(b), the pressure obtains its peak value within 10 ms of the nozzle firing. Therefore, the temporal constraints resulting from pixel saturation and the dimensions of the test chamber, as elaborated in Sec. III B, fall comfortably within the scope of plume evolution.

D. Vector images of plume-regolith interaction

Figures 19–23 compare the PIV vector images of plume-liberated high-density and low-density regolith at a regular time period of 2 ms from the moment of plume contact with the regolith surface. The nozzle is fixed at a $Y/D_e = 4$ stand-off distance at location $X/D_e = 0$, and the liberated particles are moving from the left to the right, away from the nozzle. Figure 19 shows the removal of particles from the top layer of the regolith bed. A sheet of particles ejected in the shape of a triangle can be seen from 6 ms onward for both densities. The ejection of particles adjacent to the jet axis $X/D_e = 2$ may be observed in Fig. 21 at 8 ms. The bottom of the nozzle assembly, at $Y/D_e = 4$, acts as a solid boundary that blocks the highly inclined particles from reaching higher distances. This has created a plateau-like structure in the vector field between $X/D_e = 0$ and $X/D_e = 8$, as seen in Figs. 21 and 22. The rest of the liberated particles beyond $X/D_e = 10$ continue to travel greater distances up to $X/D_e = 22$ and are only limited by the field of view of the camera lens. A positive inclination of particle ejection in all the frames indicates the ejection of particles is from the crater-like structure in the regolith bed.

The velocity magnitude is less than 50 m/s at 4 ms in Fig. 19 but obtains a maximum of 120 m/s within 8 ms in Fig. 21. Comparing Figs. 21(a) and 21(b), it is evident that the "high-velocity" zone of lower-density regolith particles covers a larger surface area than the higher-density particles. The observation also indicates that the region of high velocity is concentrated at an inclined angle in the outer region, situated far from both the nozzle and the regolith bed. Over the following time frames, the peak velocity of the ejected particles falls to less than 100 m/s. Figure 23 shows the appearance of the saturation zone close to the jet impingement region after 12 ms. The saturation region spreads to a broader area in the following frames, and at 20 ms, as shown in Fig. 24, almost half of the useful data have been lost near the impingement area.

E. Spatial variation of ejecta velocity at 8 ms from the moment of plume impingement

This section discusses the spatial distribution of the horizontal velocity component and vertical velocity component derived from a single frame frozen at 8 ms after the moment of plume impingement on the regolith surface.

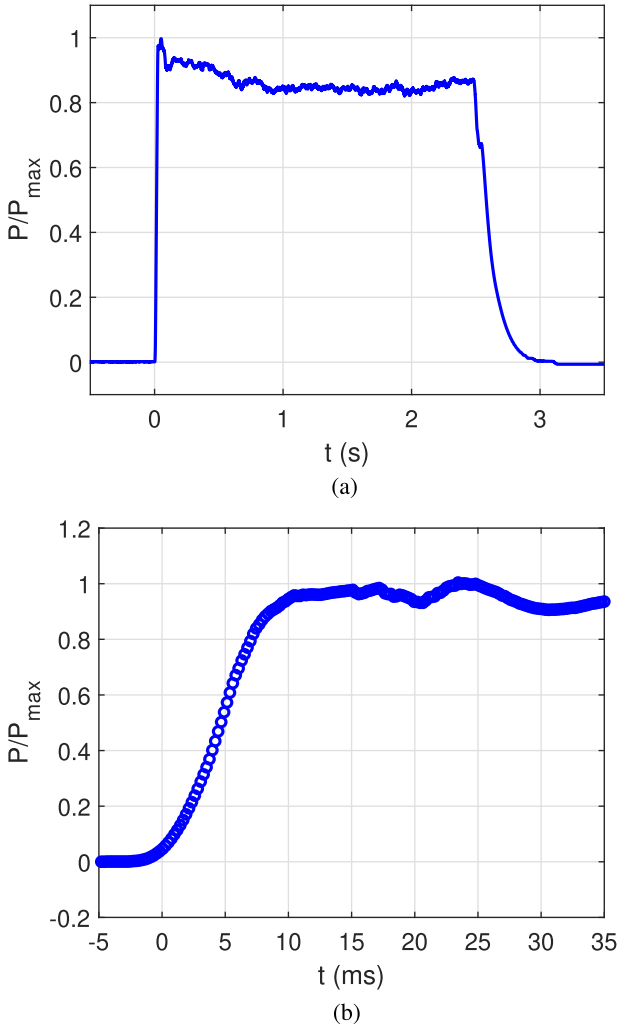

FIG. 18. Pressure profile of plume impingement for (a) the full duration and (b) the initial milliseconds.

12 February 2024 09:19:23

© Author(s) 2024

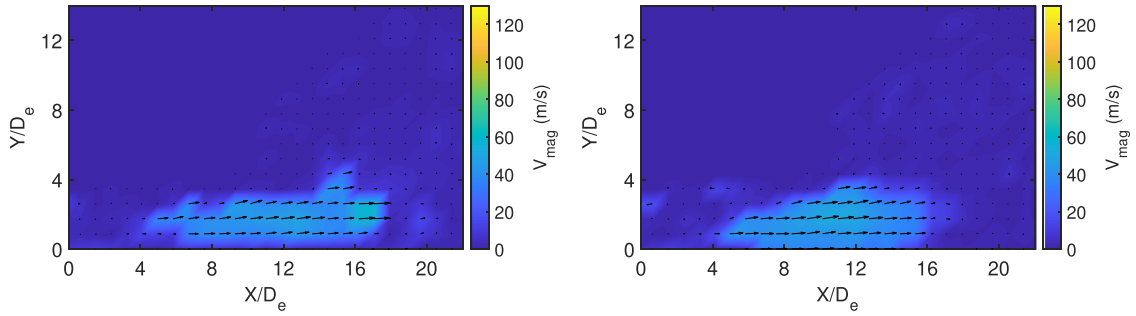

(a) High density. (b) Low density.

FIG. 19. Velocity at 4 ms.

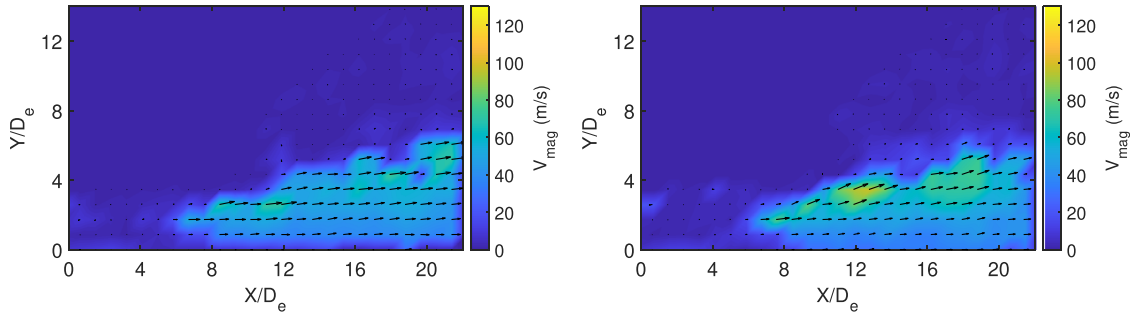

(a) High density. (b) Low density.

FIG. 20. Velocity at 6 ms.

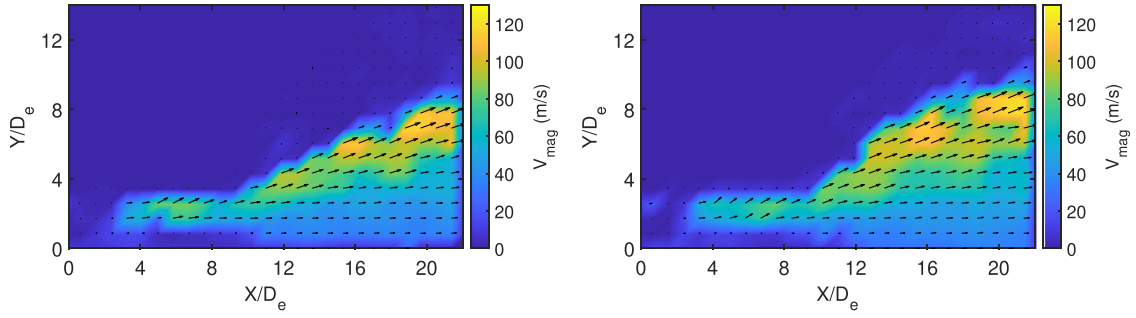

(a) High density. (b) Low density.

FIG. 21. Velocity at 8 ms.

At 8 ms, the ejection is well developed, with a zone of high-velocity particles near the outer edges for both densities, as seen from the vector field in Fig. 21. The spatial distribution of velocity components as presented in Fig. 25 is achieved by plotting extracted data along horizontal lines at $Y/D_e = 2$, 4, 6, and 8 distances from the base of the tray. Figure 26 can be referred to the horizontal lines for which the velocity components are plotted. From the plot in Fig. 25(a), both the higher and lower-density regolith simulants have the same horizontal velocity component near the surface.

However, there is a shift in the vertical velocity component between the densities in Fig. 25(b). The peak in vertical velocity observed adjacent to the nozzle suggests that particles are being expelled during the formation of the crater and that this happens closer to the nozzle centerline with the higher-density regolith simulant. At a higher vertical distance of $Y/D_e = 4$, as shown in Fig. 25(c), the horizontal velocity component for the low-density regolith material peaks at $X/D_e = 14$ away from the jet axis, while the high-density material has a slightly lower horizontal velocity component peak at a slightly

12 February 2024 09:19:23

© Author(s) 2024

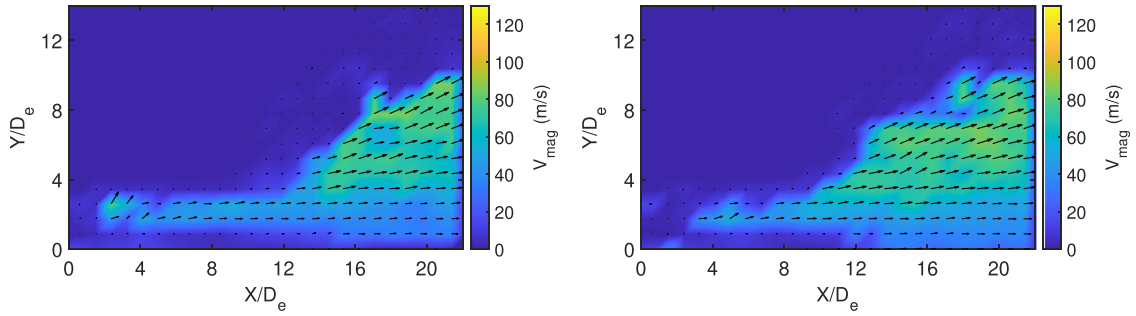

(a) High density. (b) Low density.

FIG. 22. Velocity at 10 ms.

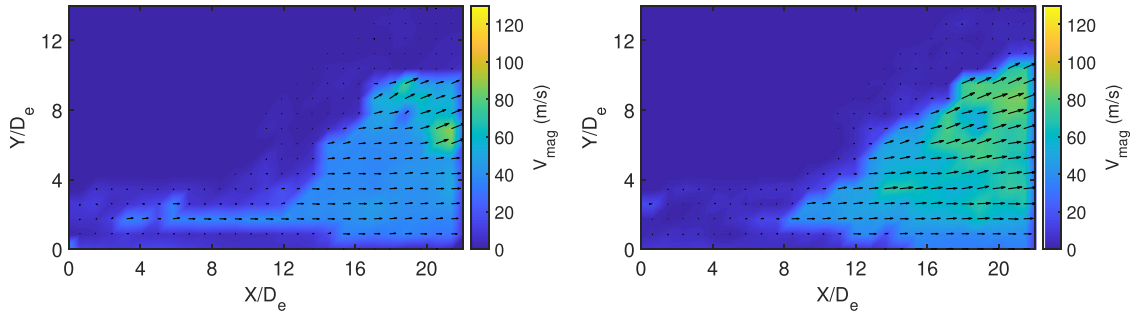

(a) High density. (b) Low density.

FIG. 23. Velocity at 12 ms.

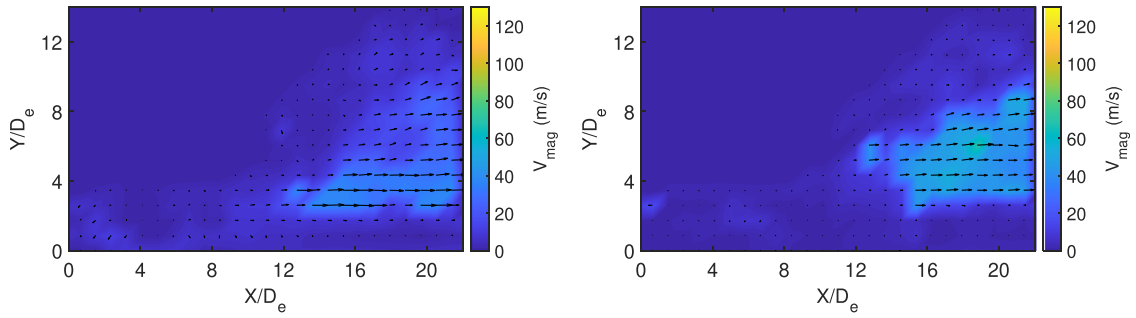

(a) High density. (b) Low density.

FIG. 24. Velocity at 20 ms.

greater radial distance. Yet, as X/D_e increases, the velocity steadily decreases and stabilizes to a constant magnitude for both densities. Regarding the vertical velocity component at $Y/D_e = 4$, it increases to a peak and then progressively decreases until it is almost zero, as shown in Fig. 25(d). Similar to the horizontal velocity component, the high-density peak is at a slightly greater radial distance.

A clear difference in the velocity due to the difference in the particle density can be seen at $Y/D_e \geq 6$ in Fig. 25(e) and in Fig. 25(f) with the lighter particles covering more area and reaching high velocity than heavier particles. The observed difference between the two densities continues at greater Y/D distances, specifically $Y/D_e = 8$ as depicted in Figs. 25(g) and 25(h). The detection of particle velocity is limited by the constraints of the lens' field of vision, rendering particles beyond a distance of $X/D_e = 22$ undetectable. However, it is evident from the preceding trends that the velocity magnitude and orientation of particle ejection increase progressively from the lowermost region and attain their maximum values at higher and far distances. The anticipated trajectory of regolith particles at the periphery of the ejected layer is that of a projectile motion, owing to the heightened velocity and acute angle of ejection. Consequently, these particles are expected to travel large distances in the context of reduced-gravity environments.

12 February 2024 09:19:23

© Author(s) 2024

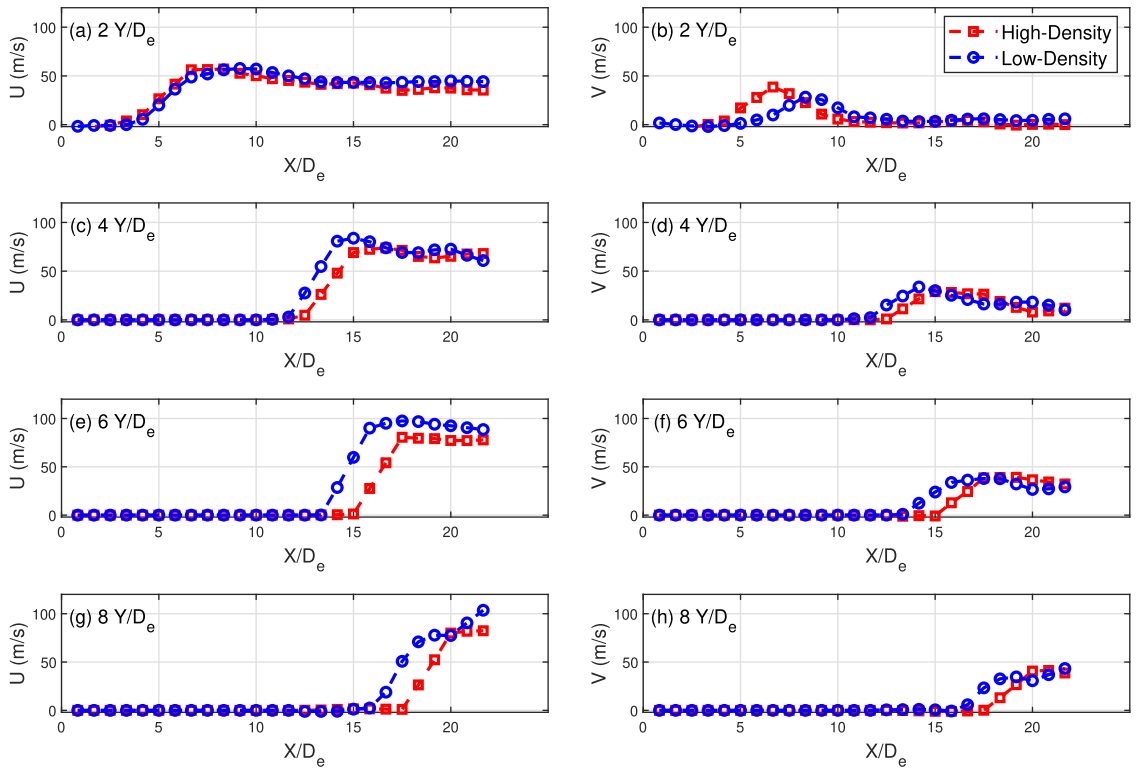

FIG. 25. Velocity components derived at different values of Y/D_e at a time frame of 8 ms from the moment of plume impingement on the regolith surface.

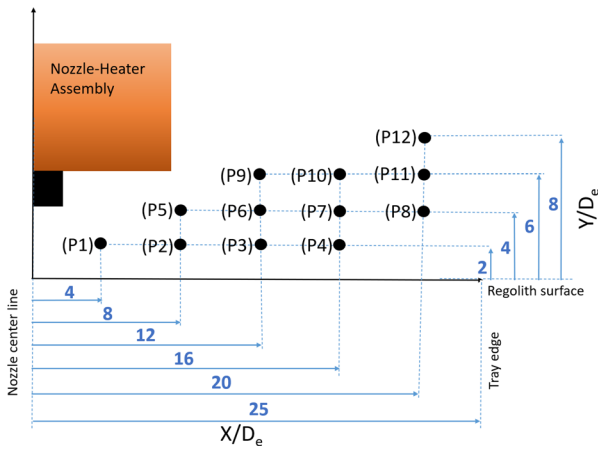

FIG. 26. Spatial points in the regolith ejection field to compute velocity and angle variation over time.

F. Temporal variations of plume-regolith interaction at different spatial points

In order to study the evolution of velocity magnitude and particle ejection angle across spatial and temporal variations, an array of points in the vector field has been established, as shown in Fig. 26. The dynamics of ejected particles at these spatial points over a time interval of 0–20 ms are plotted in Fig. 27 for velocity magnitude and in Fig. 28 for the angle of ejection. The angle of particle ejection was computed from the trigonometric ratio between the horizontal and vertical velocity components at that point, and it is measured from the horizontal regolith surface.

1. Spatial points P1, P5, and P9

*P*1 is the nearest point to the jet centerline. A momentary fluctuation in velocity can be seen for both the densities at this spatial point, as shown in Fig. 27(a), which occurs within the range of 4–16 ms with the higher density particles traveling faster than the low-density particles. However, as we move vertically to points *P*5, the velocity of the high-density particles reduces. At spatial point *P*9, the absence of high-density particle results in a zero velocity for the entire duration; however, the low-density particles spread up to this spatial point and peaked between 8 and 10 ms as shown in Fig. 27(i). The differences in how far particles spread out are caused by differences in their mass and their cohesive property. The temporal variations of the ejection angle of regolith particles at *P*1, *P*5, and *P*9 in Figs. 28(a), 28(e), and 28(i) observe the abrupt elevation of the high-density particles. The angle of ejecta in the plots implies that the particles outburst in an upward direction close to the plume impingement region, possibly from the ongoing crater formation. This proves that the surge in velocity noticed at *P*1, *P*5, and *P*9 in Fig. 27 is attributable to the contribution from the vertical component of regolith ejection originating from a crater.

12 February 2024 09:19:23

© Author(s) 2024

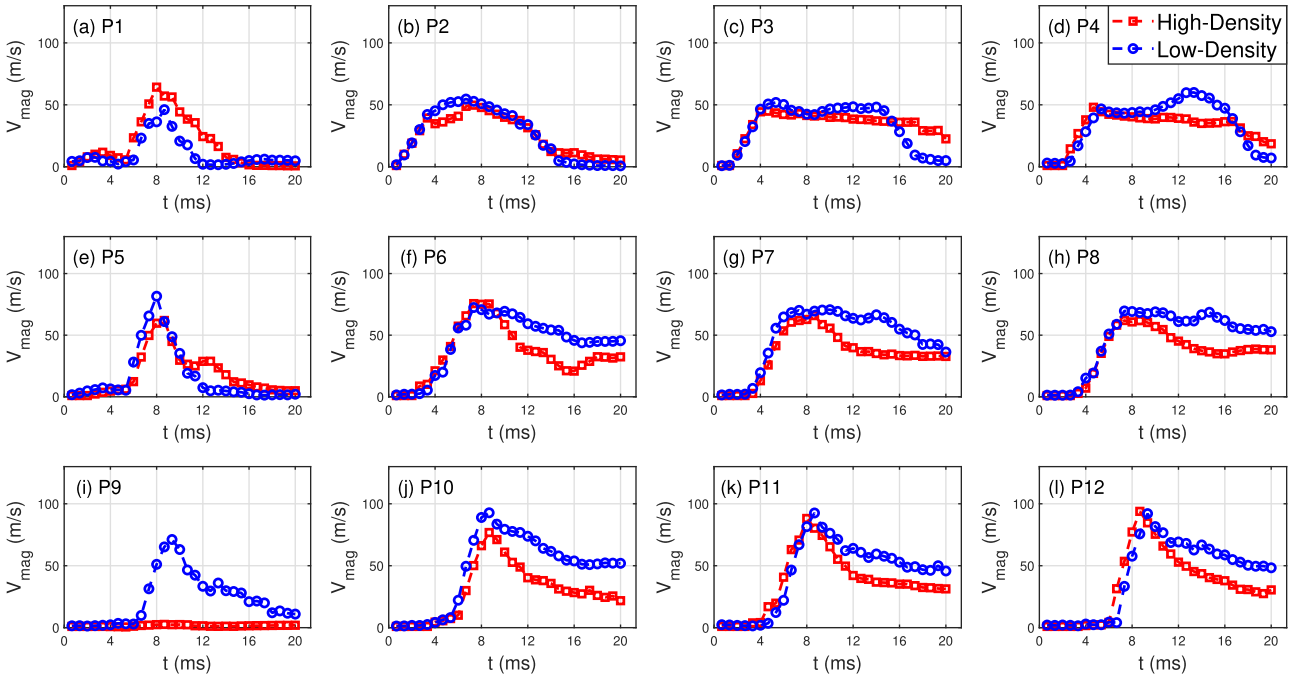

FIG. 27. Spatial and temporal variations of velocity magnitude.

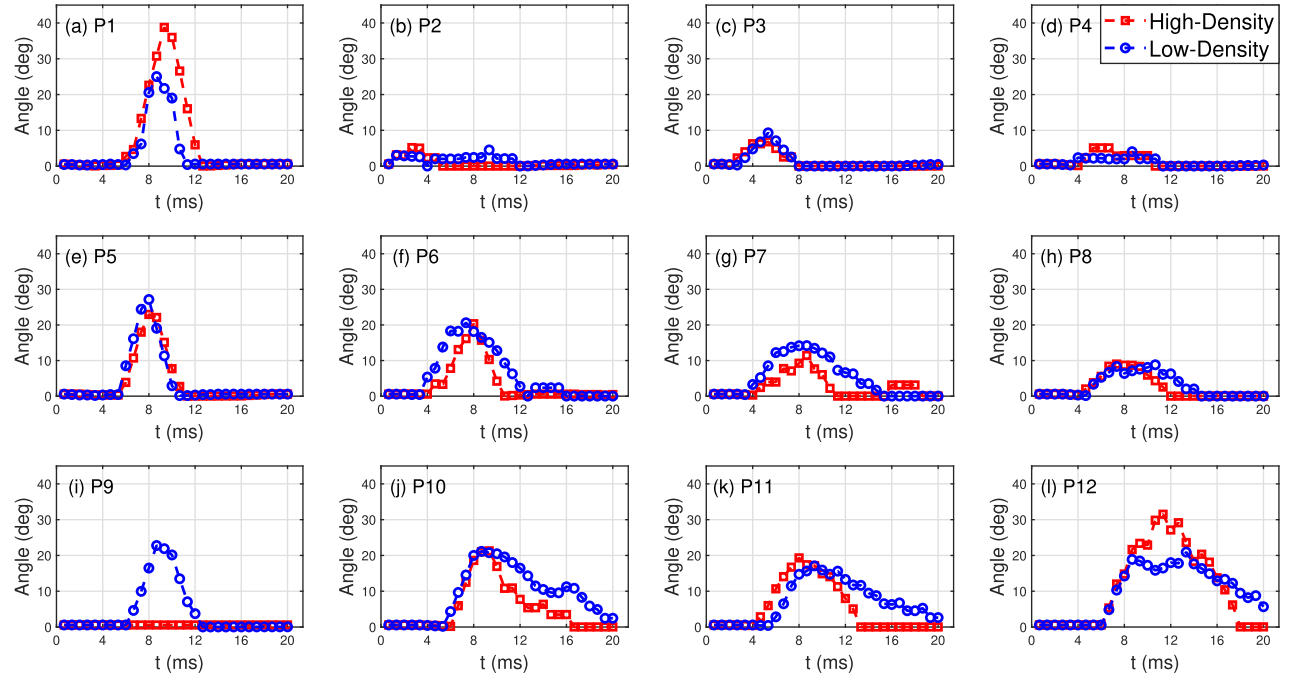

FIG. 28. Spatial and temporal variations of the inclination angle of ejected regolith.

12 February 2024 09:19:23

© Author(s) 2024

2. Spatial points P2, P3, and P4

Spatial points $P2$, $P3$, and $P4$ are parallel to the regolith surface, positioned collinearly with uniform horizontal intervals between them, located at $Y/D_e = 2$. Figures 27(b)–27(d) display the variations in the velocity of these spatial points. Both densities of particle reach a peak velocity of ∼50 m/s between 4 and 8 ms at $P2$ as shown in Fig. 27(b) and the velocity decreases and approaches zero after 16 ms. At the spatial point $P3$, depicted in Fig. 27(c), located ∼16 diameters away from the centerline of the plume, both types of particles attained their maximum velocity, which continued for a considerable duration ranging from 4 to 16 ms. Notably, the higher-density particles exhibited a gradual deceleration, whereas the low-density particles experienced a sharp decline around the 16-ms mark. The sharp decline is possibly due to pixel saturation. With the increase in the horizontal distance to $X/D_e = 20$ at spatial point $P4$, a delay in the time required to achieve peak velocity has been observed for the low-density particles. Though both particle types reached 50 m/s at 4 ms at $P4$, which is similar to the observation made at $P2$ and $P3$, the velocity of the low-density regolith simulant material continues to increase and eventually achieves a maximum at 12 ms, only to decrease afterward. Contrarily, the high-density material shows a tendency for a gradual, but continuous decline in velocity.

In comparison to the higher-density particles, the lighter particles exhibit a tendency to agglomerate at a faster rate, thereby becoming more reflective to the laser beam and expediting the saturation of pixels. The reduction in the velocity of lower-density particles toward the end of the timescale at points $P2$, $P3$, and $P4$ can be linked to the saturation of pixels resulting from the quick accumulation of the lower-density particles near the surface. The ejection angle at points $P2$, $P3$, and $P4$, in Figs. 28(b)–28(d), shows that the regolith flies horizontally parallel to the surface with virtually zero ejection angle due to the near proximity to the surface. In the early stages of the jet plume interaction, a momentary increase in the angle for a short period with a maximum of 10° may be seen.

3. Spatial points P6, P7, and P8

Figures 27(f)–27(h) show the sequential development of velocity at points $P6$, $P7$, and $P8$ at a vertical distance of $Y/D_e = 4$. At these spatial points, both particle types advance at the same rate to attain their maximum velocities at 8 ms, then a reduction in velocity is apparent in the heavier particles, while the lower-density particles maintain a larger velocity. The particle velocity magnitudes at the $Y/D_e = 4$ spatial points remain steady and above zero, in contrast to the decrease in velocity that was observed at the $Y/D_e = 2$ spatial locations. As far as the angle of ejection is concerned, from $P6$ in Fig. 28(f) to $P8$ in Fig. 28(h), a decrease in the peak angle of the ejected regolith may be seen. This shows a greater ejection angle close to the nozzle exit. The ejection angle that the lower-density regolith obtains is just slightly greater than that of the higher-density regolith.

4. Spatial points P10, P11, and P12

$P10$, $P11$, and $P12$ in Figs. 27(j)–27(l) lie in the peak velocity zone in the flow field, with the particle velocities reaching as high as 100 m/s. Both densities can be seen to obtain nearly the same peak velocity, with the lower-density particles reaching a slightly higher magnitude. Upon reaching the peak, the velocity of the higher-density particles decreases faster than those of the lower-density particles. The velocity of the lower-density regolith simulant is greater than the higher density for these three spatial points. Both densities attain a maximum ejection angle of 20° and are reduced thereafter at points $P10$, $P11$, and $P12$; however, the higher density particles suffer a high rate of reduction in angle and reach zero at $P10$ and $P11$. This could be a local event due to the deflection of particles after hitting the base of the nozzle-heater assembly. However, the higher inclination at $P12$ indicates the particles continue to travel in their inclined direction.

Upon analyzing the velocity variation at various spatial points, it is evident that the physical property of the regolith particles significantly alters the velocity of particles upon plume impingement. In addition to the fact that objects with lower mass accelerate faster compared to objects with higher mass under the same impingement force, the ongoing formation of the crater under the impinging plume can also affect the velocity at which particles are ejected at different time instances. To visualize the change in the crater properties, the image of the crater at the end of the plume impingement is captured through an IR camera, and the results are presented in Fig. 29. The use of an infrared camera enables one to observe the crater under vacuum conditions while avoiding any disruption to the regolith tray through the opening of the chamber door. The IR images show that the crater formed with the higher density regolith is shallow and narrow, while the crater formed with the lower density regolith simulant is deep and wide at the end of 2.5 s of plume impingement. A similar observation has been made in Fig. 3. The presence of a deep and wide crater indicates a higher erosion rate of the low-density regolith (possibly due to the low cohesion of the low-density particles) during the initial moments of

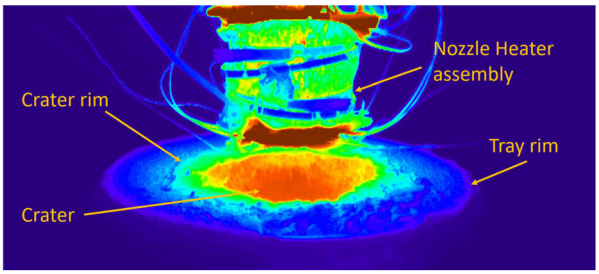

(a) Crater produced with the high density regolith simulant.

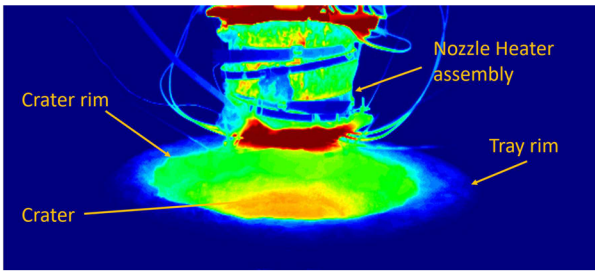

(b) Crater produced with the low density regolith simulant.

FIG. 29. Crater formation after plume impingement on a tray filled with regolith simulant, as viewed through an IR camera.

12 February 2024 09:19:23

© Author(s) 2024

ejection. This facilitates the higher entrainment of loose particles from the crater onto the surface thereby creating a difference in ejection velocity between the simulants.

In general, the acceleration phase of both densities exhibits similarity until the particles attain their maximum velocity magnitude at all spatial points. The onset of the particle acceleration varies depending on the location of the spatial points. For the spatial points close to the surface, the onset of acceleration coincides with the onset of the pressure rise measured on the flat plate in Fig. 18(b). This shows that the acceleration of particles in the early stage of plume impingement is a result of their interaction with the impinging shock wave on the surface. The momentum transfer from the impinging shock wave liberates the particles close to the surface at an equal rate irrespective of their densities. At higher spatial points, the influence of the reduced density can be seen during the deceleration phase. Upon attaining the peak velocity, the high-density particle decelerates at a higher rate than the low-density particle.

G. Close in view of plume interaction with the higher density simulant

The highly inclined ejection from the crater near the nozzle axis can be more effectively observed by directing attention toward the vicinity of the nozzle exit. To achieve this, the Samyang 135 mm wide lens was replaced with a Tokina telephoto lens with a focal length of 200 mm, and the experiment was repeated with new PIV calibration values. The regolith used in this study is the higher of the two. The telephoto lens can achieve a field of view of $X/D_e = 12$ by $Y/D_e = 8$ and for the sake of simplicity, only the result for a timeframe of 8 ms from the moment of plume-surface contact is presented in this section.

The initial moment of plume surface interaction saw two distinct ejection events, one during the initial milliseconds of particle liberation dominated by horizontal ejection velocity and later around 8 ms dominated by vertical ejection velocity in a location close to the nozzle. The vector images presented in this section capture both events in a single frame (i.e., at 8 ms from the moment of plume-surface contact).

The velocity field depicted in Fig. 30(a) exhibits a uniform distribution of the horizontal velocity component, featuring a region of elevated velocity in the upper right corner that is located far from the nozzle. The spread of particles in the "high-velocity zone" sets out on their journey shortly following the initial milliseconds of plume impingement–possibly after contact with a starting shock wave–on the undisturbed regolith bed. As the supersonic nozzle plume expands, it undergoes a starting shock. When the shock impinges normally on the surface, it leads to a strongly favorable pressure gradient (stagnation region), which causes the flow to turn outward and creates a high-velocity wall jet that travels tangentially to the surface. As the compressible wall jet extends radially outward, it forms a viscous boundary layer. The surface stresses that occur as a result of the viscous boundary layer may be greater than the cohesive strength of the soil. As a result, loose regolith may enter the wall-jet boundary layer and be transported by the accelerated gas over wider areas during the initial milliseconds. The horizontal velocity components are extracted for different Y/D_e and plotted in Figs. 31(a). The horizontal velocity components are dominant in the area close to the regolith surface, indicating that the ejecta is flowing in a surface-parallel direction.

When the stagnation pressure beneath the impinging starting shock wave exceeds the bearing capacity of the regolith, it can mechanically force the regolith downward, resulting in bearing capacity failure[53] and eventually the formation of a crater with vertical walls. The dynamic pressure of the ongoing plume behind the impinging shock wave causes the gas to penetrate into the porous structure of the regolith, which may result in the diffused gas eruption[53] with radial expulsion of gas along with regolith particles being ejected at high speed at angles aligned with the crater walls. The vertical velocity field depicted in Fig. 30(b) shows a region of high-speed particles ejecting at a high angle adjacent to the jet impingement indicating the involvement of crater-ejected particles. This high-speed upward-moving particle ejection is a separate event that occurs quickly in an ~8-ms timeframe from the moment of plume-surface contact and interacts with the nozzle assembly located at $Y/D_e = 4$ distance. This may potentially cause damage to the lander instruments in the vicinity of the nozzle in real-world landing scenarios.

The velocity components are extracted for different Y/D_e and plotted in Fig. 31(b). The vertical velocity component exhibits a significant presence in the range of $2 < X/D_e < 6$, as evidenced by Fig. 31(b). At a distance of $X/D_e = 4$, the peak vertical velocity

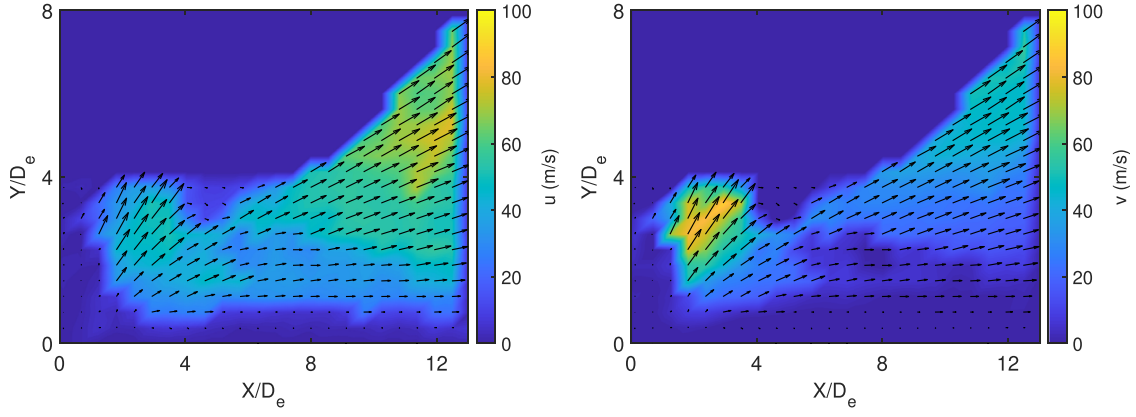

(a) Horizontal velocity component (m/s). (b) Vertical velocity component (m/s).

FIG. 30. Velocity components at 8 ms from the moment of jet-regolith interaction.

12 February 2024 09:19:23

© Author(s) 2024

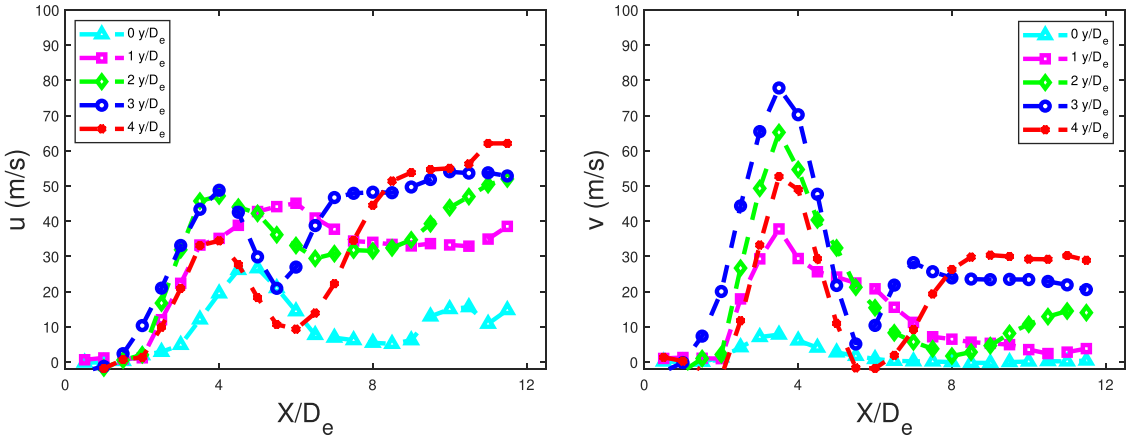

(a) Horizontal velocity component (m/s). (b) Vertical velocity component (m/s).

FIG. 31. Velocity components plotted for different values of Y/D_e.

component exceeds 80 m/s. However, it remains relatively modest and constant beyond the distance of $X/D_e = 6$.

The combined velocity magnitude distribution depicted in Fig. 32(a) includes the collective contribution of the horizontal and vertical velocity components at ∼8 ms from the moment of plume impingement on the regolith surface. With regard to the angle distribution of regolith ejection at 8 ms, shown in Fig. 32(b), it can be observed that the region where the vertical velocity component holds dominance exhibits the highest degree of deflection angle, reaching as high as 60° inclination. This angle is in close proximity to the nozzle axis, i.e., within $X/D_e = 4$. After $X/D_e = 4$, the regolith particles near the surface exhibit a parallel motion with respect to the regolith bed. The ejection angle in this region is observed to be below 10°. An increase in ejection angle, close to 30° can be observed for higher Y/D_e far from the nozzle axis. Figures 33(a) and 33(b) show the extracted velocity magnitude and ejection angle at different Y/D_e distances, respectively. As discussed earlier, the vertical component of regolith velocity ejected from the crater contributes to the increase in angle. The sharp increase in the angle of the ejection, combined with the high velocity, could directly impact spacecraft components in the vicinity of the nozzle setup. The ejection angle drops to less than 10° around $X/D_e = 6$ and increases again to a stable angle between $X/D_e = 6$ and $X/D_e = 12$.

The stream traces of liberated particles at ∼8 ms from the moment of plume surface contact are shown in Fig. 34. This reveals a ray of particles originating from the region of plume contact with the regolith surface spreading out across the entire image at angles ranging from near zero at the surface to a highly inclined angle near the nozzle axis. The presence of the nozzle assembly at $X/D_e = 4$ blocks the ejected particles and redirects their path. This is shown in the image as a downward deflection in the stream traces and is highlighted within the red circle. The deflection of stream traces far from the solid nozzle structure indicates that the deflected particles have an impact on the nearby particles. Despite the deflection, the particles continue to travel in their original direction as the distance increases due to collisions with adjacent particles.

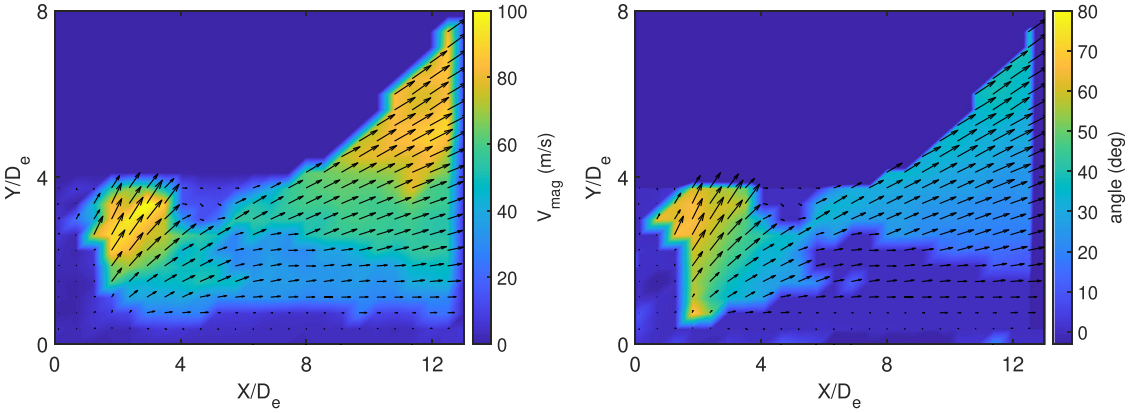

(a) Velocity magnitude (m/s). (b) Regolith ejection angle (deg).

FIG. 32. Velocity magnitude and angle of ejection at 8 ms from the moment of jet-regolith interaction.

12 February 2024 09:19:23

© Author(s) 2024

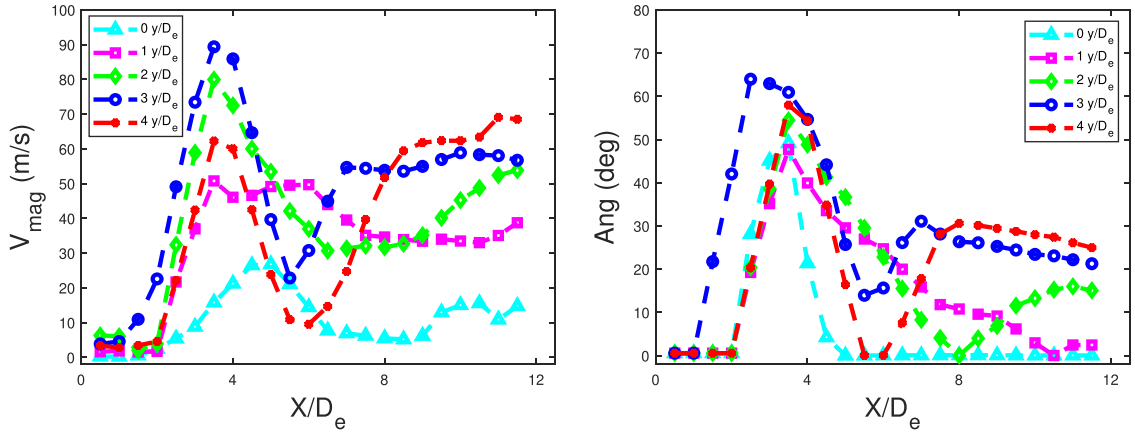

(a) Velocity magnitude (m/s). (b) Regolith ejection angle (deg).

FIG. 33. Velocity magnitude and angle of ejection plotted for different values of Y/D_e.

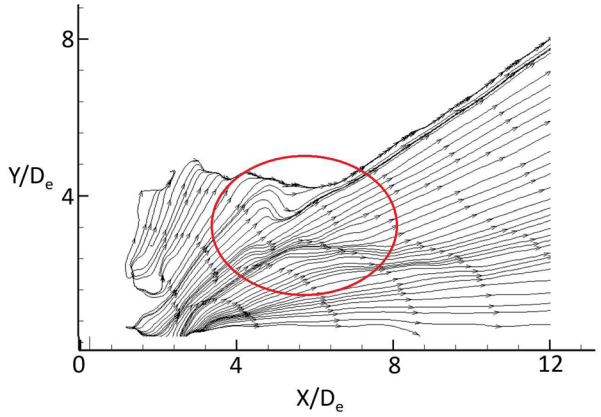

FIG. 34. Stream traces of liberated particles at 8 ms from the moment of jet impingement.

V. CONCLUSIONS

Given the future prospect of launching numerous manned and cargo missions to the moon and other airless celestial bodies in the upcoming decades, it is crucial to fully understand the dynamics of particles ejected due to lander plume interaction with regolith on extraterrestrial surfaces. This understanding is essential for accurately predicting the potential harm that may be inflicted upon lander instruments, and the close proximity of landing sites necessitates this knowledge to facilitate the construction of a permanent lunar base. Toward this goal, the current work aims to track and measure experimentally the transient phenomenon of ejected regolith from lander plume impingement in near vacuum conditions in a terrestrial laboratory environment.

To represent the "extraterrestrial" soil bed, glass microspheres of two densities, 0.46 and 0.125 g/cc, to represent the lunar and small airless body regoliths, were selected. The nozzle is heated to achieve realistic flow conditions. A pressure measurement study on an impinging plate reveals the presence of a shock wave during the initial phases of plume release, followed by a stable jet flow. The addition of a buffer tank to the test chamber ensures the chamber pressure is contained within an acceptable level to represent a landing event. The use of Schlieren could not capture the flow features in rarefied environments; consequently, an innovative approach was employed using laser illumination to visualize the initial transient moment of the plume-regolith interaction, and their results are presented.

The high-speed particle image velocimetry (HS-PIV) method was employed to compute the vectors of ejected regolith during the plume-regolith interaction event at different densities in vacuum conditions. In contrast to traditional PIV techniques that involve the introduction of seeder particles into the fluid flow, the present study employs the liberated regolith particles themselves as the seeding agent. This non-traditional approach presents novel difficulties arising from the manner in which glass particles of varying sizes disperse light in the absence of an atmospheric medium. Additionally, a higher ejection velocity, which causes a faster return of particles to the experimental area upon impact with the chamber walls, limits the duration of the experiment. The agglomeration of particles during an ejection event also limits the duration due to the saturation of pixels in the PIV image. These constraints limit the ejecta tracking to 30 ms from the moment of plume contact with the regolith surface.

However, the temporal constraints resulting from pixel saturation and the dimensions of the test chamber fall comfortably within the scope of plume evolution. The plume impingement pressure attains its peak value within a duration of 10 ms from the moment the transducer starts to register increasing pressure. In addition to this, the visualization of tracer particles from the nozzle exit reveals that the plume attains its full expansion within a time frame of ∼8 ms from the moment of nozzle firing.

The untraditional PIV method effectively captures the initial moments of transiently ejected particles in vacuum conditions. The experimental findings indicate the presence of a triangular-shaped particle sheet that spreads out from the region of plume impingement, as observed for both particle densities. The particles close to the regolith surface accelerate to a magnitude of 50 m/s within the first 4 ms of plume impingement. As time progresses, the ejection of particles at

12 February 2024 09:19:23

© Author(s) 2024

high inclinations results in the emergence of a region characterized by particles exhibiting high velocities located away from both the nozzle axis and the regolith bed. The particles in this region accelerate quickly from 0 m/s to a peak ejecta velocity of 100 m/s between 4 and 8 ms, coinciding with the rise in plume impingement pressure, possibly due to the presence of an impinging starting shock wave. Upon reaching the peak, the ejected particles gradually decelerate. Over a time period of 8–20 ms, the particles gradually attain a stable velocity. A lower ejection angle of less than 10° has been observed close to the surface of the regolith container for both densities.

It is identified that the momentum transfer from an impinging starting shock wave liberates the particles at an equal rate until they attain their peak velocity, irrespective of their difference in densities. However, after attaining the peak, the lower-density regolith simulants travel at greater speed, reach higher elevations, and cover a larger area than their higher-density counterparts.

Following the initial moment of regolith ejection, a high inclination and high-velocity ejection occur near the nozzle plume boundary at a time of around 8 ms. The dominance of the vertical component of velocity and the strongly inclined orientation of the vectors suggest that regolith particles have been ejected from a crater-like formation, possibly resulting from a bearing capacity failure of the regolith bed. Due to differences in particle flotation and cohesive properties, the lower-density particles tend to entrain large amounts of particles, resulting in wide and deep craters with slanted walls. Whereas, the crater formation for the higher-density regolith is shallow and narrow, with steep walls observed at the end of the impingement. The difference in crater slope results in a steeper angle of ejection for higher-density particles. These ejected particles can directly interact with sensitive instruments close to the nozzle installation and potentially cause damage.

Stream traces of ejected particles reveal the presence of the nozzle heater assembly at height $Y/D_e = 4$, block the ejected particles, and deflect to lower inclination angles.

ACKNOWLEDGMENTS

The authors wish to express gratitude toward the European Space Agency for funding this research ESA Contract No. 4000115469/15/NL/KML/fg, and BUSCH UK for their ongoing assistance in ensuring the efficient functioning of the facility. We also gratefully acknowledge help from Technical Services (Brian Robb, Zackary Manson) from the James Watt School of Engineering from the University of Glasgow, along with Ph.D. student Bradley Craig, for their help with the laser assembly.

AUTHOR DECLARATIONS

Conflict of Interest

The authors have no conflicts to disclose.

Author Contributions

Senthilkumar Subramanian: Formal analysis (lead); Investigation (lead); Methodology (equal); Software (equal); Validation (equal); Visualization (lead); Writing – original draft (lead); Writing – review & editing (equal). **Andrew Wilson:** Investigation (supporting); Software (equal); Visualization (equal); Writing – original draft (supporting). **Craig White:** Conceptualization (equal); Resources (equal); Supervision (equal); Validation (equal); Writing – review & editing (equal). **Konstantinos Kontis:** Conceptualization (lead); Formal analysis (supporting); Funding acquisition (equal); Investigation (equal); Methodology (equal); Project administration (lead); Resources (lead); Supervision (lead); Validation (supporting); Visualization (supporting); Writing – original draft (supporting); Writing – review & editing (supporting). **David Evans:** Formal analysis (supporting); Investigation (supporting); Methodology (equal); Resources (equal); Validation (equal). **Jeroen Van den Eynde:** Conceptualization (equal); Formal analysis (supporting); Funding acquisition (equal); Investigation (supporting); Methodology (supporting); Project administration (equal); Supervision (supporting); Validation (supporting); Visualization (supporting); Writing – review & editing (equal).

DATA AVAILABILITY

The data that support the findings of this study are available from the corresponding author upon reasonable request.

REFERENCES

[1] J. R. Gaier, "The effects of lunar dust on EVA systems during the Apollo missions," Technical Report NASA/TM—2005-213610 (NASA, 2007).
[2] S. K. Mishra, K. D. Prasad, P. Nath, D. Agarwal, S. S. Kumar, and A. Bhardwaj, "Effect of lunar landing on its surface, surrounding environment and hardware: A numerical perspective," Planet. Space Sci. **211**, 105398 (2022).
[3] I. A. Kuznetsov, A. V. Zakharov, G. G. Dolnikov, A. N. Lyash, V. V. Afonin, S. I. Popel, I. A. Shashkova, and N. D. Borisov, "Lunar dust: Properties and investigation techniques," Sol. Syst. Res. **51**, 611–622 (2017).
[4] C. M. Katzan and J. L. Edwards, "Lunar dust transport and potential interactions with power system components," Technical Report (NASA, 1991).
[5] C. W. Chen and B. D. Pollard, "Radar terminal descent sensor performance during mars science laboratory landing," J. Spacecr. Rockets **51**, 1208–1216 (2014).
[6] A. Morris, D. Goldstein, P. Varghese, and L. Trafton, "Modeling the interaction between a rocket plume, scoured regolith, and a plume deflection fence," in *Earth and Space 2012: Engineering, Science, Construction, and Operations in Challenging Environments* (American Society of Civil Engineers, 2012), pp. 189–198.
[7] X. He, B. He, and G. Cai, "Simulation of rocket plume and lunar dust using DSMC method," Acta Astronaut. **70**, 100–111 (2012).
[8] A. B. Morris, D. B. Goldstein, P. L. Varghese, and L. M. Trafton, "Approach for modeling rocket plume impingement and dust dispersal on the moon," J. Spacecr. Rockets **52**, 362–374 (2015).
[9] A. B. Morris, D. B. Goldstein, P. L. Varghese, and L. M. Trafton, "Lunar dust transport resulting from single-and four-engine plume impingement," AIAA J. **54**, 1339–1349 (2016).
[10] C. White, T. Scanlon, J. Merrifield, K. Kontis, T. Langener, and J. Alves, "Numerical and experimental capabilities for studying rocket plume-regolith interactions," AIP Conf. Proc. **1786**, 170003 (2016).
[11] A. Rahimi, O. Ejtehadi, K. Lee, and R. Myong, "Near-field plume-surface interaction and regolith erosion and dispersal during the lunar landing," Acta Astronaut. **175**, 308–326 (2020).
[12] J. West, P. Liever, A. Weaver, T. P. Shurtz, M. Gale, W. C. Krolick, and L. W. Griffin, "Overview of the predictive simulation capability element of the plume surface interaction project," AIAA Paper No. 2022-2319, 2022.
[13] C. White, M. K. Borg, T. J. Scanlon, S. M. Longshaw, B. John, D. R. Emerson, and J. M. Reese, "dsmcFoam+: An openFOAM based direct simulation Monte Carlo solver," Comput. Phys. Commun. **224**, 22–43 (2018).
[14] Z. Cao, M. Agir, C. White, and K. Kontis, "An open source code for two-phase rarefied flows: RarefiedMultiphaseFoam," Comput. Phys. Commun. **276**, 108339 (2022).

12 February 2024 09:19:23

© Author(s) 2024

[15]Z. Cao, C. White, M. B. Agir, and K. Kontis, "Lunar plume-surface interactions using rarefiedMultiphaseFoam," Front. Mech. Eng. **9**, 1116330 (2023).
[16]H. Zhang, C. Li, J. You, X. Zhang, Y. Wang, L. Chen, Q. Fu, B. Zhang, and Y. Wang, "The investigation of plume-regolith interaction and dust dispersal during chang'E-5 descent stage," Aerospace **9**, 358 (2022).
[17]J. E. Lane, P. T. Metzger, C. D. Immer, and X. Li, "Lagrangian trajectory modeling of lunar dust particles," in *Earth & Space 2008: Engineering, Science, Construction, and Operations in Challenging Environments* (American Society of Civil Engineers, 2008), pp. 1–9.
[18]G. Cai, L. Liu, B. He, G. Ling, H. Weng, and W. Wang, "A review of research on the vacuum plume," Aerospace **9**, 706 (2022).
[19]N. S. Land and L. V. Clark, *Experimental Investigation of Jet Impingement on Surfaces of Fine Particles in a Vacuum Environment* (National Aeronautics and Space Administration, 1965).
[20]N. S. Land and H. F. Scholl, *Scaled Lunar Module Jet Erosion Experiments*, Vol. 5051 (National Aeronautics and Space Administration, 1969).
[21]L. D. Jaffe, "Blowing of lunar soil by Apollo 12: Surveyor 3 evidence," Science **171**, 798–799 (1971).
[22]D. Brownlee, W. Bucher, and P. Hodge, "Primary and secondary micrometeoroid impact rate on the lunar surface: A direct measurement," Analysis of surveyor 3 material and photographs returned by Apollo 12 **284**, 143 (1972).
[23]J. N. Mpagazehe, K. W. Street, Jr., I. R. Delgado, and C. F. Higgs III, "An experimental study of lunar dust erosive wear potential using the JSC-1AF lunar dust simulant," Wear **316**, 79–91 (2014).
[24]A. C. Wittbrodt and P. T. Metzger, "Material damage from impacts of lunar soil particles ejected by the rocket exhaust of landing spacecraft," Technical Report (2008).
[25]C. Bühler, "Experimental investigation of lunar dust impact wear for different grain sizes and impact angles," in *IEEE Aerospace Conference* (IEEE, 2017), pp. 1–14.
[26]M. Kuhns, P. Metzger, A. Dove, J. Byron, S. Lamb, T. Roberson, L. Lohman, W. Chambers, G. Rixon, R. Kuhns *et al.*, "Deep regolith cratering and plume effects modeling for lunar landing sites," in *Earth Space 2021* (American Society of Civil Engineers, 2021), pp. 62–78.
[27]P. Metzger, A. Dove, M. Conroy, J. Gloria, A. O'Reilly, and A. St John, "Ejecta sheet tracking, opacity, and regolith maturity (Ejecta STORM): An instrument for lunar landing plume effects and dust dynamics," in *52nd Lunar and Planetary Science Conference, LPI Contribution No. 2548* (Lunar and Planetary Institute, 2021), 2616.
[28]C. J. Eberhart, J. West, and A. M. Korzun, "Overview of plume-surface interaction data from subscale inert gas testing at NASA MSFC test stand 300 vacuum facilities," AIAA Paper No. 2022-1811, 2022.
[29]A. M. Korzun, C. J. Eberhart, J. West, P. Liever, A. Weaver, J. Mantovani, A. Langton, B. Kemmerer, and A. Atkins, "Design of a subscale, inert gas test for plume-surface interactions in a reduced pressure environment," AIAA Paper No. 2022-1808, 2022.
[30]J. S. Rubio, M. Gorman, M. X. Diaz-Lopez, and R. Ni, "Plume-surface interaction physics focused ground test 1: Setup and preliminary results," AIAA Paper No. 2022-1810, 2022.
[31]M. X. Diaz-Lopez, M. Gorman, J. S. Rubio, and R. Ni, "Plume-surface interaction physics focused ground test 1: Diagnostics and preliminary results," AIAA Paper No. 2022-1810, 2022.
[32]O. K. Tyrrell, R. J. Thompson, P. M. Danehy, C. J. Dupuis, M. M. Munk, C. P. Nguyen, R. W. Maddock, T. W. Fahringer, W. C. Krolick, A. Weaver *et al.*, "Design of a lunar plume-surface interaction measurement system," AIAA Paper No. 2022-1693, 2022.
[33]M. Smith, D. Craig, N. Herrmann, E. Mahoney, J. Krezel, N. McIntyre, and K. Goodliff, "The artemis program: An overview of NASA's activities to return humans to the moon," in *IEEE Aerospace Conference* (IEEE, 2020) pp. 1–10.
[34]H. K. Athanasopoulos, "The moon village and space 4.0: The 'open concept' as a new way of doing space?," Space Policy **49**, 101323 (2019).
[35]G. Dettleff and M. Grabe, "Basics of plume impingement analysis for small chemical and cold gas thrusters," in *Models and Computational Methods for Rarefied Flows* (RTO/NATO, Rhode St. Genese, Belgium, 2011), pp. 1–40.
[36]R. T. Driftmyer, "A correlation of freejet data," AIAA J. **10**, 1093–1095 (1972).
[37]C. White, H. Zare-Behtash, K. Kontis, T. Ukai, J. Merrifield, D. Evans, I. Coxhill, T. Langener, and J. Van den Eynde, "Test facility to investigate plume-regolith interactions," in International Conference on Flight Vehicles, Aerothermodynamics and Re-Entry Missions and Engineering (FAR), 2019.
[38]E. Slyuta, "Physical and mechanical properties of the lunar soil (a review)," Sol. Syst. Res. **48**, 330–353 (2014).
[39]E. A. King, Jr., J. C. Butler, and M. Carman, Jr., "The lunar regolith as sampled by Apollo 11 and Apollo 12: Grain size analyses, modal analyses, and origins of particles," in *Proceedings of the Lunar Science Conference* (The MIT Press, 1971), Vol. 2, p. 737.
[40]D. S. McKay, G. Heiken, A. Basu, G. Blanford, S. Simon, R. Reedy, B. M. French, and J. Papike, "The lunar regolith," in *Lunar Sourcebook* (Cambridge University Press, 1991), Vol. 567, pp. 285–356.
[41]J. C. Graf, "Lunar soils grain size catalog," Technical Report (National Aeronautics and Space Administration, 1993).
[42]D. Stoeser, D. Rickman, and S. Wilson, "Design and specifications for the highland regolith prototype simulants NU-LHT-1M AND-2M," Technical Report (National Aeronautics and Space Administration, 2011).
[43]B. Gundlach and J. Blum, "A new method to determine the grain size of planetary regolith," Icarus **223**, 479–492 (2013).
[44]C. M. Schrader, D. Rickman, C. McLemore, and J. Fikes, "Lunar regolith simulant user's guide," Technical Report (National Aeronautics and Space Administration, 2010).
[45]H. Nakashima, Y. Shioji, K. Tateyama, S. Aoki, H. Kanamori, and T. Yokoyama, "Specific cutting resistance of lunar regolith simulant under low gravity conditions," J. Space Eng. **1**, 58–68 (2008).
[46]See www.3m.com/microspheres for "Energy and advanced materials division (2007)," Technical Report.
[47]R. Kuzmin, T. Shingareva, and E. Zabalueva, "An engineering model for the phobos surface," Sol. Syst. Res. **37**, 266–281 (2003).
[48]V. S. Engelschiùn, S. Eriksson, A. Cowley, M. Fateri, A. Meurisse, U. Kueppers, and M. Sperl, "EAC-1A: A novel large-volume lunar regolith simulant," Sci. Rep. **10**, 5473 (2020).
[49]W. D. Carrier, *The Four Things You Need to Know about the Geotechnical Properties of Lunar Soil* (Lunar Geotechnical Institute, 2006).
[50]M. Kiuchi and A. M. Nakamura, "Relationship between regolith particle size and porosity on small bodies," Icarus **239**, 291–293 (2014).
[51]Y. Nagaashi, T. Aoki, and A. M. Nakamura, "Cohesion of regolith: Measurements of meteorite powders," Icarus **360**, 114357 (2021).
[52]L.-O. Heim, J. Blum, M. Preuss, and H.-J. Butt, "Adhesion and friction forces between spherical micrometer-sized particles," Phys. Rev. Lett. **83**, 3328 (1999).
[53]P. T. Metzger, C. D. Immer, C. M. Donahue, B. T. Vu, R. C. Latta III, and M. Deyo-Svendsen, "Jet-induced cratering of a granular surface with application to lunar spaceports," J. Aerosp. Eng. **22**, 24–32 (2009).

12 February 2024 09:19:23

© Author(s) 2024